Wireless optoelectronic photometers for monitoring neuronal dynamics in the deep brain

Luyao Lu[a,b,1], Philipp Gutruf[a,b,1], Li Xia[c,1], Dionnet L. Bhatti[d,e,1], Xinying Wang[f], Abraham Vazquez-Guardado[g,h], Xin Ning[a], Xinru Shen[a], Tian Sang[a], Rongxue Ma[a], Grace Pakeltis[a], Gabriel Sobczak[c], Hao Zhang[b], Dong-oh Seo[d,e], Mantian Xue[a], Lan Yin[i], Debashis Chanda[g,h], Xing Sheng[j,2], Michael R. Bruchas[c,d,e,k,l,2], and John A. Rogers[a,b,m,n,o,p,q,r,s,t,2]

[a]Department of Materials Science and Engineering, Frederick Seitz Materials Research Laboratory, University of Illinois at Urbana–Champaign, Urbana, IL 61801; [b]Department of Materials Science and Engineering, Northwestern University, Evanston, IL 60208; [c]Department of Biomedical Engineering, Washington University School of Medicine, St. Louis, MO 63130; [d]Washington University Pain Center, Washington University School of Medicine, St. Louis, MO 63130; [e]Department of Anesthesiology, Washington University School of Medicine, St. Louis, MO 63130; [f]Department of Electrical and Computer Engineering, University of Illinois at Urbana–Champaign, Urbana, IL 61801; [g]Center for Research and Education in Optics and Lasers, The College of Optics and Photonics, University of Central Florida, Orlando, FL 32816; [h]NanoScience Technology Center, University of Central Florida, Orlando, FL 32826; [i]School of Materials Science and Engineering, Tsinghua University, Beijing 100084; [j]Department of Electronic Engineering, Tsinghua University, Beijing 100084, China; [k]Department of Neuroscience, Washington University School of Medicine, St. Louis, MO 63110; [l]Division of Biology and Biomedical Sciences, Washington University School of Medicine, St. Louis, MO 63110; [m]Department of Biomedical Engineering, Northwestern University, Evanston, IL 60208; [n]Department of Chemistry, Northwestern University, Evanston, IL 60208; [o]Department of Mechanical Engineering, Northwestern University, Evanston, IL 60208; [p]Department of Electrical Engineering and Computer Science, Northwestern University, Evanston, IL 60208; [q]Simpson Querrey Institute, Northwestern University, Evanston, IL 60208; [r]Feinberg School of Medicine, Northwestern University, Evanston, IL 60208; [s]Department of Neurological Surgery, Northwestern University, Evanston, IL 60208; and [t]Center for Bio-Integrated Electronics, Northwestern University, Evanston, IL 60208

Contributed by John A. Rogers, December 21, 2017 (sent for review October 30, 2017; reviewed by Polina Anikeeva and Xiangfeng Duan)

Capabilities for recording neural activity in behaving mammals have greatly expanded our understanding of brain function. Some of the most sophisticated approaches use light delivered by an implanted fiber-optic cable to optically excite genetically encoded calcium indicators and to record the resulting changes in fluorescence. Physical constraints induced by the cables and the bulk, size, and weight of the associated fixtures complicate studies on natural behaviors, including social interactions and movements in environments that include obstacles, housings, and other complex features. Here, we introduce a wireless, injectable fluorescence photometer that integrates a miniaturized light source and a photodetector on a flexible, needle-shaped polymer support, suitable for injection into the deep brain at sites of interest. The ultrathin geometry and compliant mechanics of these probes allow minimally invasive implantation and stable chronic operation. In vivo studies in freely moving animals demonstrate that this technology allows high-fidelity recording of calcium fluorescence in the deep brain, with measurement characteristics that match or exceed those associated with fiber photometry systems. The resulting capabilities in optical recordings of neuronal dynamics in untethered, freely moving animals have potential for widespread applications in neuroscience research.

neuroscience | photometry | optogenetics

Monitoring neural dynamics with cellular, anatomical, and time-locked specificity in freely moving animals represents a critically important capability in elucidating connections between neuronal processes and behaviors, a goal of modern neuroscience research. Optical methods exploit genetically encoded calcium indicators (GECIs) (1–3) as fluorescence labels of cellular dynamics (4–12). The advent of fiber photometry recording platforms provide some important capacity for performing such measurements in animals during behaviors (6,7) associated with anxiety, social interactions (e.g., mating and fighting), and motor control (e.g., head motion, jumping, and wheel running). The required fiber-optic waveguides tend to impede movements, thereby restricting studies of natural behaviors. Motion artifacts that are often imposed upon the animals or introduced into the recorded signals must be carefully monitored. Furthermore, mismatches between the mechanical properties of the soft, compliant tissues of the brain and the hard, rigid fiber probes result in unavoidable tissue damage with potential for implant detachment (13, 14).

Here, we present a compact, integrated wireless photometry system for deep-brain fluorescence recordings that avoids these disadvantages by leveraging concepts in injectable optoelectronic devices originally introduced in the context of optogenetics (15–17). These platforms include an ultrathin, flexible, and lightweight injectable probe with active components for stimulating and recording fluorescence, interfaced to a detachable transponder, a control unit, and a miniature power supply for communication with an external receiver system. Such systems record and digitize fluorescence signals from a targeted area of the deep brain and broadcast the resulting signals wirelessly, thereby avoiding physical tethers and associated motion artifacts. Systematic experiments in multiple animal studies demonstrate capabilities for

Significance

Wireless systems for imaging/recording neuronal activity in untethered, freely behaving animals have broad relevance to neuroscience research. Here, we demonstrate a thin, flexible probe that combines light sources and photodetectors into a platform with submillimeter dimensions, capable of direct insertion into targeted regions of the deep brain. This system allows wireless stimulation and recording of fluorescence associated with genetically encoded calcium indicators, with unique capabilities in visualizing neuronal activity. Studies using unconstrained, freely moving animal models in two different behavioral assays demonstrate the robust, reliable operation of these devices and allow comparisons to traditional photometry systems based on fiber-optic tethers to external light sources and detectors.

Author contributions: L.L., P.G., L.X., D.L.B., X. Sheng, M.R.B., and J.A.R. designed research; L.L., P.G., D.L.B., X.W., A.V.-G., X.N., X. Shen, T.S., R.M., G.P., G.S., H.Z., D.-o.S., M.X., L.Y., D.C., X. Sheng, and M.R.B. performed research; L.L., P.G., L.X., D.L.B., M.R.B., and J.A.R. analyzed data; and L.L., P.G., L.X., D.L.B., M.R.B., and J.A.R. wrote the paper.

Reviewers: P.A., Massachusetts Institute of Technology; and X.D., University of California, Los Angeles.

Conflict of interest statement: J.A.R. and M.R.B. are involved in a company, Neurolux, Inc., that offers different, but related, products to the neuroscience community.

Data deposition: Code used for operation and analysis in this study is available on GitHub (https://github.com/PhilippGutruf/Wireless-implantable-optoelectronic-photometers-for-monitoring-neuronal-dynamics-in-the-deep-brain).

[1]L.L., P.G., L.X., and D.L.B. contributed equally to this work.

[2]To whom correspondence may be addressed. Email: xingsheng@tsinghua.edu.cn, bruchasm@wustl.edu, or jrogers@northwestern.edu.

This article contains supporting information online at www.pnas.org/lookup/suppl/doi:10.1073/pnas.1718721115/-/DCSupplemental.

monitoring neural activity in diverse behavioral assays that are widely used in neuroscience, including foot-shock tests and pharmacological stimulations, while detecting calcium dynamics in the basolateral amygdala (BLA), a deep-brain structure involved in emotional processing. The results provide proof-of-concept examples of the capture of neural activity with genetically defined spatiotemporal precision in targeted deep-brain regions in freely moving animals, with reduced displacement and damage to brain tissue compared with fiber photometry approaches. The combined advantages in size, weight, signal quality, chronic stability, multiplexed data collection, and ability to operate with untethered animals over large areas suggest the potential for broad applications in neuroscience research.

Results

Wireless Photometry System Design. Fig. 1*A* presents an exploded schematic illustration of the injectable photometry probe. This component of the system includes a microscale inorganic light-emitting diode (μ-ILED; 270 × 220 × 50 μm) and a related device for photodetection (μ-IPD; 100 × 100 × 5 μm) placed adjacent to one another (separation ∼ 10 μm; Fig. 1 *B*, *Right* and *SI Appendix*, Fig. S1) on a thin, narrow, and flexible polyimide (PI) substrate (thickness 75 μm). A narrow-band absorber (140 × 140 × 7 μm) photolithographically defined on top of the μ-IPD serves as an optical filter to block light from the μ-ILED and to pass photons at the wavelength of the fluorescence. Lithographically patterned metal films (total thickness ∼ 1 μm) serve as electrical interconnects. A coating (thickness ∼ 10 μm) of polydimethylsiloxane (PDMS) encapsulates the system (*SI Appendix*, Fig. S2). Detailed information on the fabrication steps appears in *SI Appendix*, Fig. S3 and *Materials and Methods*. Fig. 1*B* shows an optical image of a probe terminated in a flexible flat cable (FFC) connector (*Left*) and a colorized scanning electron microscope (SEM) image of the tip end (*Right*). Fig. 1 *C*, *Upper* and *SI Appendix*, Fig. S4 provide a schematic illustration of the overall multilayer layout and geometry of the μ-IPD (15).

The injectable part of the probe has a maximum thickness of ∼150 μm (at the location of the μ-ILED), a width of ∼350 μm, and a length of ∼6 mm (adjustable to match the targeted anatomy). By comparison, state-of-the-art fiber photometry implants use multimode fibers with core diameters ranging from 200 to 400 μm and outer diameters from 230 to 480 μm (6, 7, 18–20); most reported studies use fibers with core diameters >400 μm. The injectable probes of Fig. 1*B* displace volumes of tissue that are comparable to those associated with the smallest photometry fibers (∼230-μm outer diameters) and at the same time offer performance comparable to the largest (400-μm core sizes), as discussed in detail later. The bending stiffness of the injectable probe is 6.48×10^{-8} and 1.59×10^{-8} N·m^2 along the width and thickness directions, respectively (21, 22). These values are between two and three orders of magnitude lower than those of even the smallest fibers (1.00×10^{-5} N·m^2 for a 230-μm outer diameter optical fiber, where the Young's modulus of the silica core is used for the outer layer). Such differences are important

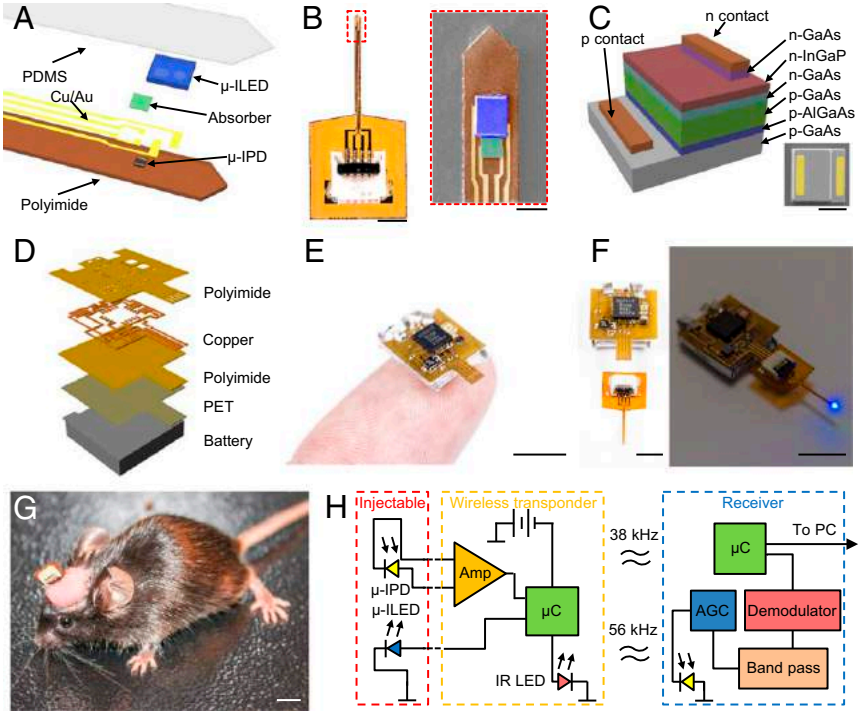

Fig. 1. Miniaturized, ultrathin, lightweight wireless photometry systems for deep-brain Ca^{2+} measurements. (*A*) Schematic exploded-view illustration of a wireless, injectable, ultrathin photometry probe with a μ-ILED and a μ-IPD at the tip end. (*B*, *Left*) Optical micrograph of the injectable photometry probe. The tip has a total width of ∼350 μm and a thickness of ∼150 μm. The weight is 29 mg. (*B*, *Right*) Magnified colorized SEM image of the tip (orange, PI; yellow, interconnection; blue, μ-ILED; green, μ-IPD with an optical filter). [Scale bars, 2 mm (*Left*) and 200 μm (*Right*).] (*C*, *Upper*) Schematic illustration of a GaAs μ-IPD. (*Lower*) SEM image of a representative μ-IPD (lateral dimensions of 100 × 100 μm^2 and thickness of 5 μm). Metal electrodes are colorized in yellow. (Scale bar, 50 μm.) (*D*) Schematic exploded-view illustration of a transponder. (*E*) Photographic image of the wireless detachable transponder on fingertip. (Scale bar, 1 cm.) (*F*) Images of the separated transponder and injectable (*Left*) and the integrated system in operation (*Right*). The transponder is connected only during signal recording. [Scale bars, 4 mm (*Left*) and 8 mm (*Right*).] (*G*) Image of a freely moving mouse with a photometry system (1 wk after surgery). (Scale bar, 7 mm.) (*H*) Schematic illustration of the electrical operating principles of the system: Read out and control occur with a detachable wireless transponder that also facilitates signal amplification and digitalization. The signal is transmitted via an IR-LED with a modulation frequency of 38 kHz for single-transponder operation and an additional 56 kHz in dual-transponder operation. A receiver system demodulates the signal and sends the received data to a PC for data storage.

because decreases in bending stiffness reduce the tissue damage that can result from micromotions of the implanted probes relative to the brain tissue (13).

Fig. 1 *D* and *E* shows a schematic diagram of the layered architecture of the transponder and a picture of a transponder on a fingertip, respectively. *SI Appendix*, Fig. S5 presents an image of a cannula from a fiber photometry system for size comparison. Small outline resistors, capacitors, a low-power microcontroller (μC 4 × 4 mm) and amplifiers (1.42 × 1.42 mm), together with a low-power infrared (IR) wireless communication module, serve as the basis of a small, lightweight transponder. Fig. 1*F* shows a transponder, an injectable probe (*Left*), and their operation (*Right*). The probe and the entire system have masses of 29 mg and 0.5 g. By comparison, the masses of an optical cannula and a patch cord are 0.43 and 9.5 g, respectively (*SI Appendix*, Fig. S6). Other types of head-mounted devices have considerably larger masses, typically >1 g (4, 5), than those reported here. An adult mouse can easily accommodate the probe and the transponder (Fig. 1*G*), without any apparent change in behavior. The probe inserts easily into the brain, by using standard fixtures. The transponder is removable, such that it can be attached only when needed.

Fig. 1*H* presents a schematic illustration of the electrical operation. A photovoltaic amplification scheme conditions signals from the μ-IPD (*SI Appendix*, Fig. S7). The μC (low-power small-outline AtTiny84) on the transponder activates the μ-ILED and samples signals from the operational amplifier. An IR LED transmits data to a wireless receiver system via a 38- and 56-kHz modulated carrier frequency and amplitude key shifting. These two carrier frequencies are compatible with a wide range of commercial integrated receivers. False data packets as well as incomplete transfers are avoided with a checksum. A lightweight rechargeable polymer lithium ion battery provides power for up to 2 h of continuous operation at a sampling rate of 27 Hz. The removable design for the transponder and battery allows, via separate charging steps, behavioral studies that extend over long periods of time. The signal broadcast by the wireless transponder is captured by an independent automatic gain control, bandpass, and demodulator to yield digital signals that pass to a μC (ATmega328P) embedded in a custom circuit that includes a USB connection. This circuit decodes the signals, time-stamps the measurement, and sends them to a personal computer for evaluation.

Electrical and Optical Properties. Characterization studies of separate μ-IPDs and μ-ILEDs reveal the key operational properties of each component and illustrate their roles in the overall performance of the system (*SI Appendix*, Fig. S8). *SI Appendix*, Fig. S9 shows the current vs. voltage characteristics of the μ-IPD and μ-ILED. The emission maximum wavelength is at 470 nm (*SI Appendix*, Fig. S10), well matched to the fluorescence excitation source for many GECIs, including GCaMP6 (3, 23). The μ-IPD has a high external quantum efficiency (EQE) (maximum value of 88%) from 350 to 850 nm, with an EQE value of 44.4% at 512 nm after application of the thin-film optical filter, respectively (Fig. 2*A*). The filter absorbs photons from 465 to 490 nm (Fig. 2*B*), with a rejection ratio of transmitted photons at 512 nm (maximum fluorescence emission wavelength of GCaMP6) to those at 470 nm of 98.6%, thereby minimizing the influence of the μ-ILED emission light on the measured signals (Fig. 2*A*). Given that most of the photons from the μ-ILED travel in a direction directly opposite to the μ-IPD, and the leakage through the filter only represents a small, largely time-independent background, this rejection ratio is sufficient to do fluorescence microscopy, as confirmed by in vivo results in freely behaving animals discussed later. Selective detection of photons at other wavelengths (e.g., red) can be achieved simply by using alternative optical filters.

The thermal load on the brain tissue represents an important consideration for in vivo operation. Previous studies using injectable μ-ILEDs for optogenetics reveal that increases in temperature are only ∼0.2 °C when the μ-ILED operates with an output power of 10 mW/mm^2 and a duty cycle of 20% (24). For the photometry system, the μ-ILED operates at a much lower optical power (240 μW) with the same duty cycle of 20%; thus the thermal influence is minimal, as confirmed by simulation results where temperature increases are proportional to the blue light power (25). Devices remain fully functional after being immersed in PBS at 37 °C over 38 d. Accelerated tests show that the encapsulated probes survive (as determined by intermittent operation) for 4 and 10 d of immersion in PBS at 90 °C and 75 °C, respectively (*SI Appendix*, Fig. S11). These findings suggest lifetimes of ∼5 mo at 37 °C in PBS solution, by using extrapolations based on the Arrhenius equation. *SI Appendix*, Fig. S12 presents an image of a working device after implantation in the BLA area of mice for ∼2 mo.

The digital IR wireless data transmission scheme provides low-power operation (<15 mW during continuous sensing and broadcasting operation) with a small overall size (1 cm^2 lateral dimensions and thickness of 0.4 mm) and lightweight construction (0.5 g for the transponder, including battery). The system operates most efficiently in a line-of-sight mode, but it can also exploit indirect transmission achieved by reflection from objects in the surroundings. The robustness of the data connection can be illustrated by mapping the data rates with the transponder facing all cardinal directions in non-line-of-sight scenarios across a large (60 × 60 cm) open cage equipped with one sensor in each corner and with a closed nontransparent housing that is equipped with a single sensor. Data rates remain stable for all positions at ∼28 Hz with 12-bit packet size (336 bits per s) and transponder orientations, thereby demonstrating angle-independent operation for practical situations of interest to animal studies (*SI Appendix*, Fig. S13). A transparent analog to this test environment is displayed in Fig. 2*C* to highlight sensor position and system operation in such a scenario. Fig. 2*D* shows the receiver system paired with a standard home cage for a mouse. The hardware requirements here are significantly less cumbersome compared with those for fiber photometry systems (*SI Appendix*, Fig. S14).

An essential aspect of the technology is that it eliminates all external connecting electrical lines and fibers, and it bypasses conventional bulk optical instrumentation from fiber photometry. In addition to the removal of motion artifacts, this mode of operation allows concurrent recordings from multiple, freely moving animals simultaneously without risk for entanglement or animal manipulation of the interconnect lines. Here, a wireless injectable probe and a transponder unit with a unique broadcasting frequency can be applied to each animal in a population, thereby allowing study of complicated behavioral questions associated with social interactions. Fig. 2*E* presents in vitro recording results collected simultaneously from two separate wireless photometers over time, each operating at a different carrier frequency and modulation coding (38 kHz NEC and 56 kHz RC5) to ensure no cross-over loss. The demonstration involves use of an external green light source to stimulate both photodetectors temporally offset, showing uninterrupted data transmission with stable data rates during dual recordings. As expected, both μ-IPDs (red and gray traces in Fig. 2*E*) exhibit stable baselines under ambient light and the same increase in analog-to-digital converter (ADC) values for illumination with a green LED above each probe for 1 s, which represents the fluorescence intensity after amplification. Fig. 2*F* shows an image of two freely moving mice with head-mounted wireless photometers enclosed by protective housings (0.3 g; *SI Appendix*, Figs. S6 and S14).

Fluorescence signals from intracellular calcium levels spanning values typical of neurons at rest (0.05–0.1 μM) and when stimulated (10 μM) (26) can be captured with a linearity in response (R^2 = 0.991) comparable to that of advanced fiber photometry platforms (R^2 = 0.995) when using Oregon Green 488

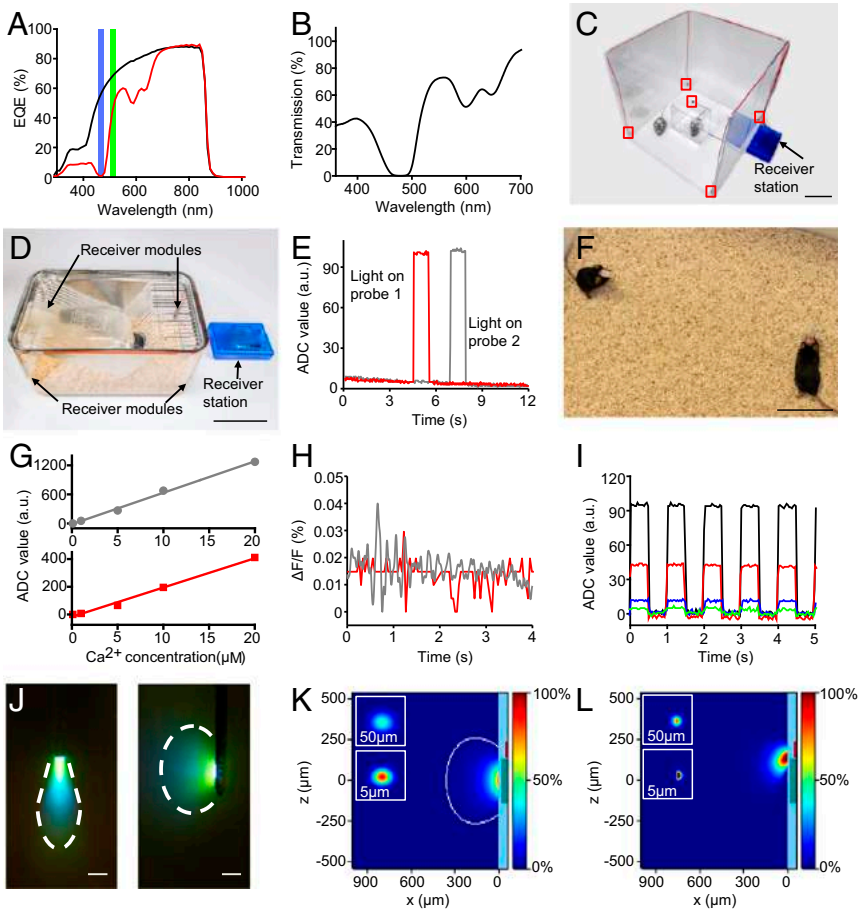

Fig. 2. Electrical and optical properties of wireless photometry systems. (*A*) EQE spectra of a μ-IPD with (red) and without (black) a narrow band absorber on top. The blue and green areas highlight wavelength ranges with strong emission from the μ-ILED and fluorescence of GCaMP6f, respectively. (*B*) Transmission spectrum of 7-μm-thick layer of SU-8 with 1.5 wt % absorber. (*C*) A system demonstration with the receiver system outfitted to a cage with an enclosure inside the test area. The receivers are marked with a red box. (Scale bar, 10 cm.) (*D*) A standard mouse home cage outfitted with the receiver system. (Scale bar, 10 cm.) (*E*) Demonstration of simultaneous recordings of two wireless photometry systems, where an external green LED is turned on for 1 s at different time periods on top of gray and red traced probes, respectively. (*F*) Two freely moving mice each implanted with a wireless photometry system and housing for simultaneous recordings in a behavior box. (Scale bar, 7.5 cm.) (*G*) Measurement of fluorescence intensity in calcium indicator (excitation maximum, 494 nm; emission maximum, 523 nm) solutions with different Ca^{2+} concentrations (from 0.1 to 20 μM) by the fiber-optic system (*Upper*; gray) and the wireless photometry probe (*Lower*; red). (*H*) Comparison of fluorescence signal fluctuations over time in a 10 μM Ca^{2+} solution normalized to the dynamic range shown in *G* between the fiber (gray) and wireless system (red). (*I*) Wireless probe responses to simulated fluorescence with defined green light intensities from an external green light LED source. Optical intensities are 4.5×10^{-3}, 1.1×10^{-2}, 2.9×10^{-2}, and 5.7×10^{-2} mW/cm^2 for the green, blue, red, and black curves, respectively. (*J*) Microscopic photograph comparison of the florescence profiles (outlined in white) of a conventional fiber photometry probe (*Left*) and the injectable photometry probe (*Right*). (Scale bars, 800 μm.) (*K*) Normalized emission intensity profile with 1% contour for the μ-ILED as a function of depth in brain tissue. (*K*, *Insets*) Emission intensity at positions 5 and 50 μm above the encapsulated μ-ILED. (*L*) Spatial distribution of fluorescence captured by the μ-IPD as a function of depth in brain tissue. (*L*, *Insets*) Fluorescence intensity at positions 5 and 50 μm from the top edge (the edge closest to the μ-ILED) of encapsulated μ-IPD.

BAPTA-2 as the calcium indicator (Fig. 2*G*). These results demonstrate that the overall changes in fluorescence associated with a normal range of functions of neurons fall into the measured dynamic range of both systems. Fig. 2*H* shows the fluctuations in measured fluorescence over time for the two systems. Here, differences in fluorescence recorded between an initial measurement and subsequent times in a 10 μM Ca^{2+} solution (maximum Ca^{2+} in vivo) define the baseline noise, or intrinsic fluctuations in the measurement. These values can be compared with the full-scale fluorescence dynamic range associated with solutions at concentrations of 0.1 μM (at rest) to 10 μM Ca^{2+} (under stimulation), as defined by the difference between the highest recorded ADC value at 10 μM Ca^{2+} and the lowest recorded ADC value at 0.1 μM Ca^{2+}. When tested side by side, the wireless and fiber photometry platforms show comparable noise relative to dynamic range used to measure the in vitro Ca^{2+} signals. When examining the noise closely, the noise in the fiber system appears to be largely of analog nature, while the signal of the wireless system is mostly limited by the ADC (12 bit). In addition, the autofluorescence from the PI substrate of the wireless system is orders of magnitude smaller in intensity than the fluorescence associated with the 0.1 μM Ca^{2+} solution under the same excitation condition (488 nm laser; *SI Appendix*, Fig. S15). Since the μ-ILED emits light opposite to the PI substrate, the influence of the autofluorescence from the substrate on in vivo measurement is further minimized, confirmed by the low noise equivalent power (NEP) value of the wireless photometry system as discussed below.

Fig. 2*I* shows the recorded signals from a wireless photometer under controlled illumination with a green LED light source (maximum emission at 527 nm). The NEP of the wireless photometry system can be determined by reducing the intensity of the green light until the measurement yields a signal-to-noise ratio (SNR) of 1 at a frequency of 1 Hz (27). This type of measurement defines an

NEP of ~4.1×10^{-14} W for the wireless photometer. By comparison, the Newport femtowatt silicon photoreceiver alone (model no. 2151) used in certain commercial fiber photometry systems exhibits a NEP of ~1.9×10^{-14} W at 527 nm (calculated from online technical specification). The overall NEP value for the fiber photometry system will be similar to the NEP for the photoreceiver due to other noise and loss, such as a low transfer efficiency in fluorescence throughput to detector from fiber tip (~20% in one reported case for fiber bundles) (4). The SNR of the wireless probe to 527-nm green light is 92.6 under a 5.8×10^{-2} mW/cm^2 light power.

The probing volumes associated with wireless and fiber photometers are different due to distinct patterns of optical excitation and modes for collection of fluorescent light. Fig. 2*J* shows comparisons based on measurements obtained by placing the photometers in a fluorescent solution with 5 μM $CaCl_2$ and 0.3 μM Oregon Green 488 BAPTA-2 calcium indicator (emission maximum at 505 nm when excited at 488 nm; *SI Appendix*, Fig. S15*A*). The fiber exhibits a conical illumination pattern with a low divergence angle centered at the tip of the fiber, relevant to the adjacent volume, from which fluorescence is also collected. The wireless injectable system involves a divergent illumination pattern normal to the surface of the μ-ILED and lateral to the long axis of the probe. A fraction of this illuminated volume generates fluorescence capable of capture by the μ-IPD. Optical simulation of the two systems in brain tissues using GCaMP6 as calcium indicator and previously reported optical density, absorption coefficient, and scattering coefficient of brain tissues provide insights into the details (28–30). The wireless photometry system model consists of an emulated brain tissue superstrate and a PDMS encapsulation for both the μ-ILED and μ-IPD. In these calculations, the μ-ILED exhibits a full emission angle of ~70° and a numerical aperture (NA) of 0.78, while the fiber photometry system (diameter 400 μm) shows an emission angle of 42° and an NA of 0.48. The penetration depths for blue light (defined as the depth where the emission power from the light source decreases to 1% of initial value) are 360 and 500 μm for the wireless and fiber photometers, respectively (Fig. 2*K* and *SI Appendix*, Fig. S16*A*). The latter value is comparable to that of a previous report (31). The illumination volumes (defined as the volume where the emitted power is >1% of initial value) for the μ-ILED and optical fiber are 5.3×10^7 and 1.2×10^8 μm^3, respectively. The difference mainly results from the increased dimensions of the optical fiber (400-μm core diameter) in comparison with the dimensions of μ-ILED ($220 \times 270 \times 50$ μm). Fig. 2*L* and *SI Appendix*, Fig. S16*B* present the spatial distribution of captured fluorescence, showing the different nature of fluorescence collection. The μ-IPD has a large NA of 1.35, and it measures fluorescence signals with spatial origins that coincide with its acceptance angle. The overlap of this volume with that illuminated by the μ-ILED determines the spatial distribution of the recorded fluorescence. In addition to the sizes and optical characteristics of the μ-IPD and μ-ILED, their spatial proximity influences this quantity. For the probes reported here, the main measurement volume lies above the interface between the μ-ILED and μ-IPD due to the overlap between the fluorescence emission volume and acceptance angle of the μ-IPD (Fig. 2*L*). The ability to adjust this shape and size of this volume through engineering design of the layout can be used to tune the performance of the system. The fiber photometry system stimulates and collects fluorescence in volumes located directly at the fiber end face, without similar flexibility in design. Details of the optical simulation appear in *SI Appendix*, Note S1. *SI Appendix*, Table S1 provides a systematic comparison of different parameters between the wireless and fiber photometry systems.

Wireless Photometry Devices Improve Natural Behavior in Chronically Implanted, Freely Moving Animals. For in vivo application, the injectable wireless probe can be chronically implanted into the rodent brain to monitor calcium transient activity in any brain region expressing a dynamic fluorescent protein, such as a GECI. The detachable nature of the wireless transponder reduces the effect of the weight of the wireless photometry system on the mice (Fig. 3*A*) during periods when recording is not necessary. Mice with the integrated photometry system implanted into the BLA (i.e., chronically implanted device and attachable transponder) socially interact with novel conspecifics in an unfamiliar environment more frequently compared with mice implanted with a photometry-based fiber optic and tethered by a connecting cable identical to that used for recording (Fig. 3 *B*–C, and *D*). Additionally, wireless photometer-implanted mice travel more distance during an open field test (OFT) (Fig. 3 *E* and *F* and *SI Appendix*, Fig. S17*B*) and spend more time in the center zone of the apparatus compared with mice implanted with traditional fiber optic (Fig. 3*G*). Chronic implantation of either device, however, without the attachable transponder or tethering, does not alter motor coordination in the rotarod test (*SI Appendix*, Fig. S17 *C* and *D*). These results indicate that the use of a wireless photometry system allows animals to generally move more freely and lowers anxiety-like behavior during the OFT compared with a fiber-optic system, which would be an advantage when recording neural activity during naturalistic, ethologically relevant behaviors.

Additionally, immunohistochemical analysis reveals that the implantable wireless photometry probe requires a smaller cross-sectional area to emit light into the BLA (Fig. 3 *H* and *I* and *SI Appendix*, Fig. S17 *E* and *H*). Furthermore, the wireless photometry probe lesions significantly less brain tissue and has a similar immunoreactive glial response compared with fiber-optic probes after 4 wk since deep brain implantation (Fig. 3 *J*–*L*), indicative of normal immunoglial responses.

Wireless Monitoring of Calcium Transient Activity in the BLA During Aversive and Pharmacological Stimuli. Monitoring and recording calcium transients in the BLA of mice expressing a virally mediated genetically encoded calcium indicator (AAV5-CaMKII-GCaMP6f) provides proof-of-concept evidence to evaluate the general utility of the wireless photometry system (Fig. 4*A*). Calcium transients as measured by a GECI are strongly correlated with neuronal activity dynamics, as recently reported (32, 33). The BLA is an important hub for processing emotional information and is especially responsive in rodents during negative affective states, such as fear and anxiety-like states, that are brought about by stressors (34–36). Following implantation of either the fiber or wireless systems, we record calcium transients in excitatory BLA neurons in vivo during salient behavioral perturbations, with one active recording session for each mouse. Recordings from multiple animals in an identical experimental scenario serve as the basis for comparisons. Simultaneous recordings from a single animal using both fiber and wireless devices is not possible due to the small size of the BLA region. The optical powers for stimulation from the μ-ILED (240 μW) and fiber tip are comparable to ensure fair comparison between the two systems. The low optical power minimizes photobleaching of GCaMP6 (7, 18).

Fig. 4*A* shows a mouse with a wireless device recording calcium transients in CaMKII-expressing BLA neurons during an aversive, unpredictable foot-shock test. The SNR for each recording system is calculated as the peak dF/F divided by SD of baseline signal (Fig. 4*B*), which does not show significant difference. Both fiber photometry (Fig. 4 *C* and *D*) and wireless photometry (Fig. 4 *E* and *F*) systems detect increases in fluorescence within the BLA after shock administration, indicative of a shock-induced increase in BLA neuronal activity. From the heatmap in Fig. 4 *D* and *F*, it is clear that some mice show immediate responses to the foot shock, while others have some delays in the recorded calcium transients for both systems. Additionally, both groups show significantly increased frequency of calcium

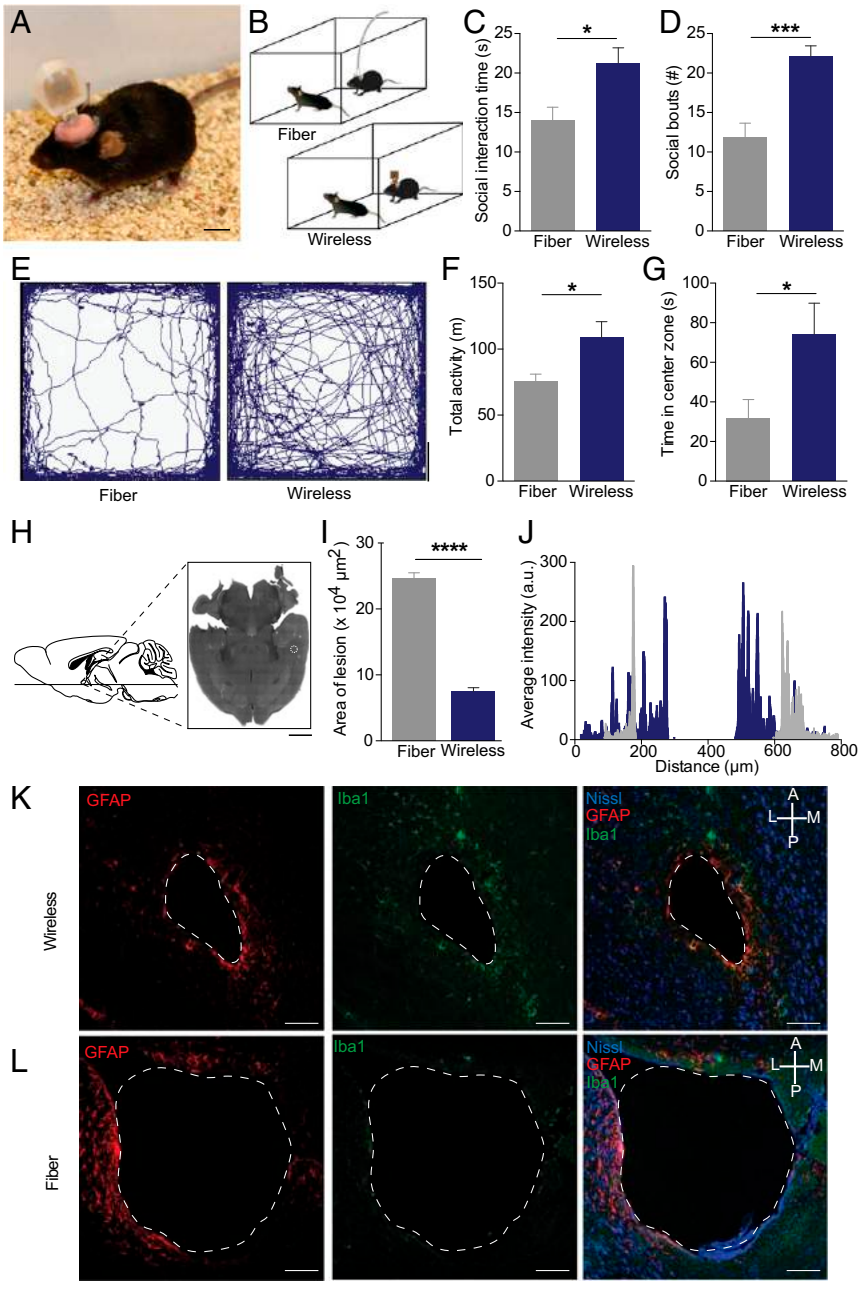

Fig. 3. Wireless photometry systems are compatible with awake, freely behaving mice. (*A*) Photographic image of a mouse in behavioral arena with wireless photometry system affixed. (Scale bar, 1 cm.) (*B*) Cartoon of social interaction task. (*C* and *D*) Mice implanted with miniaturized, lightweight wireless photometry probes display increased social interaction time (*C*) and number of interaction bouts (*D*) compared with mice implanted and tethered using traditional fiber photometry systems ($n = 10$, fiber; $n = 9$, wireless). $^{*}P = 0.01$; $^{***}P = 0.0003$ [two-tailed t test, $t_{(17)} = 4.560$]. (*E*) Representative traces of total activity in an open field arena for mice implanted with each device. (Scale bar, 10 cm.) (*F* and *G*) Mice implanted with wireless photometry probes display increased traveled distance, a measure of activity (*F*; $n = 12$ per group), and increased time spent in the center zone, a measure of anxiety-like behavior, in the open field compared with fiber-implanted mice (*G*; $n = 12$ per group). (*F*) $^{*}P = 0.02$ [unpaired two-tailed t test, $t_{(22)} = 2.478$]. (*G*) $^{*}P = 0.03$ [unpaired two-tailed t test, $t_{(22)} = 2.262$]. (*H*) Schematic and confocal image of the mouse brain at the point of observation of tissue damage for lesion and inflammation measurements from wireless neural probe. (Scale bar, 2 mm.) (*I*) Wireless photometry probes lesion less brain tissue compared with traditional photometry probes ($n = 3$ per group; three slices per mouse). $^{****}P < 0.0001$ (unpaired two-tailed t test). (*J*) Representative linescan of fluorescence intensity of glial cell markers from traditional and wireless photometry probes. (*K* and *L*) Representative confocal fluorescence images of horizontal amygdalar slices. Minimal inflammatory glial responses occur after implantation of both the wireless and fiber photometry probes, as shown by immunohistochemical staining of astrocytes (GFAP; red) and activated microglia (Iba1; green). (Scale bars, 100 μm.)

"spike events" (events per minute) in the 25 s following shock delivery compared with the baseline recording (Fig. 4*G*).

To further demonstrate the utility of the wireless photometry devices to reliably detect calcium transient activity changes following pharmacological manipulation, we investigate the BLA network dynamics, following stimulation of a receptor known to be expressed on CaMK2+ neurons within the BLA. The β-adrenergic receptor system in the amygdala has been demonstrated to be an integral part of negative affective processing through its ability to modulate anxiety and fear responses in both rodents and humans (35–38). Therefore, understanding how this receptor system modulates the network activity of amygdalar neurons helps to further elucidate discrete information about negative affective processing. Here, we use both the wireless photometry and traditional fiber-optic systems to examine neural activity in the BLA during activation of β-adrenergic receptors. Administration of isoproterenol (4 mg/kg, i.p.), a selective β-adrenoreceptor agonist, increases the frequency of fluorescence signal events per minute in the BLA in both fiber and wireless photometry systems (Fig. 4 *H* and *I*). The observation of events per minute in both systems is not meant as a direct comparison; rather, it demonstrates the sensitivity of signal detection of both fiber and wireless photodetector-based systems. Isoproterenol administration significantly increases the incidence of calcium transient events compared with baseline and saline controls in both systems (Fig. 4*J*). These results suggest that the wireless photometry system is highly biocompatible and efficiently collects fluorescence dynamics in freely moving animals during behavior.

Discussion

The lightweight, wireless photometry technology introduced here allows monitoring of fluorescent activity dynamics in deep-brain structures in freely moving animals. By comparison with platforms

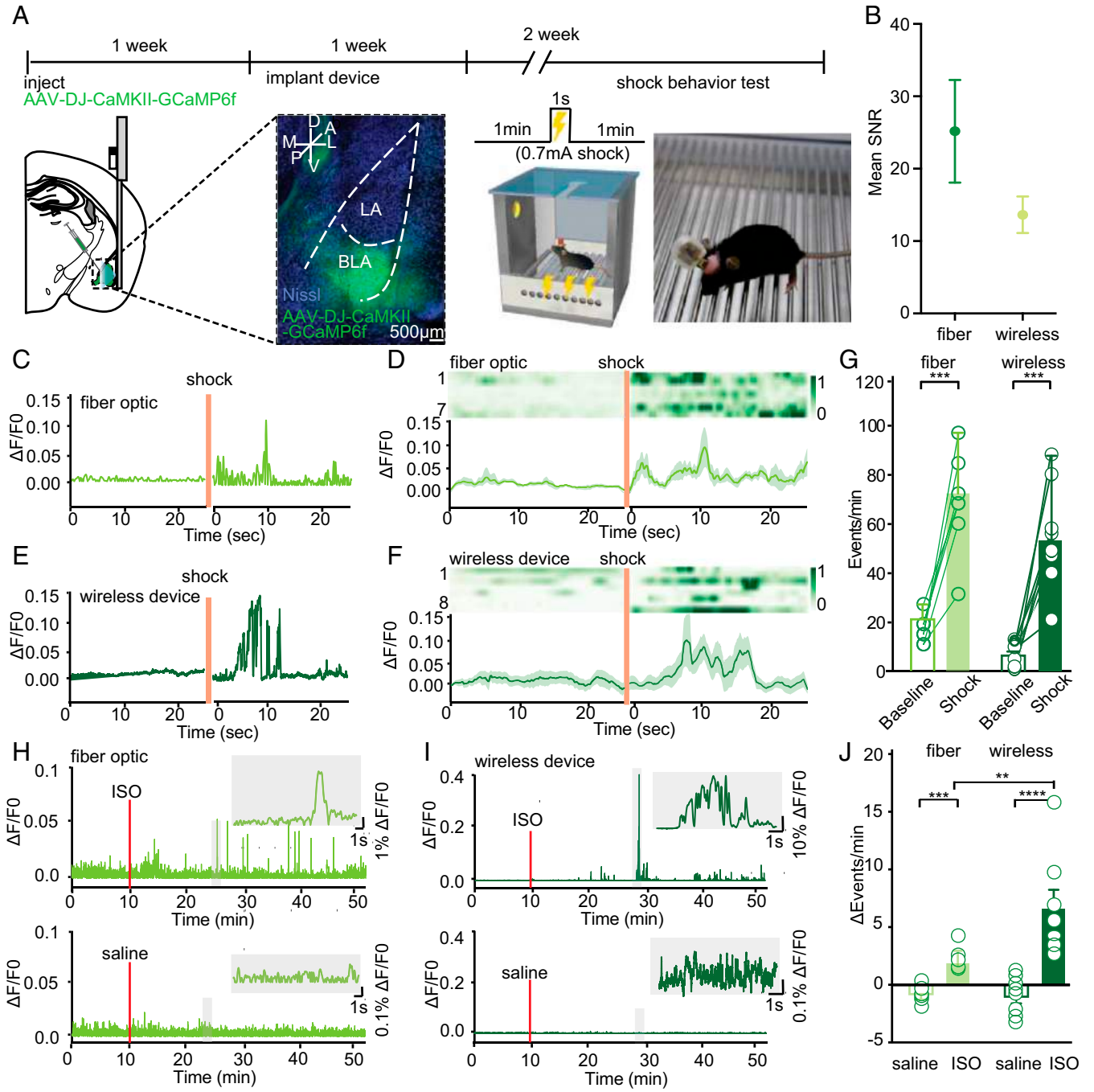

Fig. 4. Wireless in vivo detection of calcium transient activities in the BLA. (*A*, *Upper*) Timeline of virus injection, device implantation, and behavior test. (*A*, *Lower*) Schematic of viral delivery and expression of AAV-DJ-CaMKII-GCaMP6f (shown in green) into the BLA and wireless delivery of 473-nm light; diagram of shock delivery and cartoon for a mouse with wireless device during behavior in the shock apparatus; and free-moving mice with a wireless device in the shock box. (*B*) SNR was calculated as the peak dF/F divided by the SD of the baseline dF/F. There is no significant difference between the two systems [$n = 13$, unpaired t test, $t_{(11)} = 1.632$, $P = 0.1309$]. (*C*) A sample trace showing fluorescence change before and after shock of an animal using the fiber photometry system. (*D*) Heatmap (*Upper*) for seven trails of signals recorded by fiber optics before and after shock, aligned with trace plotted as mean (curves) ± SEM (shading around curves) (*Lower*). Fluorescence signals are normalized for each trail. Darker colors indicate higher fluorescence signal. (*E*) A sample trace showing fluorescence change before and after shock of an animal using the wireless photometry system. (*F*) Heatmap (*Upper*) for eight trails of signals recorded by wireless device before and after shock, aligned with trace plotted as mean (curves) ± SEM (shading around curves) (*Lower*). (*G*) Spike events frequency in the BLA before (baseline)/after shock in signals recorded by fiber (light green)/wireless (dark green) photometry systems. Postshock signals (filled bars) have significantly higher events frequency compared with preshock signals (open bars) recorded from fiber photometry system [$n = 7$; paired t test, $t_{(6)} = 6.978$, $P = 0.0004$], and wireless photometry system [$n = 8$; paired t test, $t_{(7)} = 6.468$, $P = 0.0002$]. (*H*, *Upper*) Fluorescence trace showing that injection of isoproteronol i.p. activates CaMKII+ BLA populations recorded by fiber photometry system. (*H*, *Lower*) Trace shows signals recorded by saline injection as control. Zoomed-in wave shapes from the dot frame are shown by side. (*I*, *Upper*) Fluorescence trace showing injection of isoproteronol i.p. activates CaMKII+ basolateral amygdalar populations recorded by wireless photometry system. (*I*, *Lower*) Trace shows signals recorded by saline injection as control. Zoomed-in wave shapes from the dot frame are shown by side. (*J*) Events frequency change (Δevents per min) before/after saline (open bars)/ISO (filled bars) for signals recorded from fiber photometry system (light green) and wireless system (dark green). Signal has a significantly higher Δevents per min for ISO injection in both systems [$n = 14$, unpaired t test, $t_{(14)} = 4.973$, $P = 0.0002$ for fiber photometry system; $n = 12$, unpaired t test, $t_{(12)} = 5.915$, $P < 0.0001$ for wireless photometry system].

for fiber photometry, these systems are small and compact, with significantly reduced requirements in supporting equipment. The cost of wireless photometry technology is significantly lower than fiber photometry. The overall cost of the wireless photometry system, including an injectable probe, a transponder, a receiver station, and fabrication, is less than $100 [US dollars (USD)] (*SI Appendix*, Table S2), while the cost for a fiber photometry system is more than $20,000 (USD) (based on the system used in this work). The essential advances follow from the concept of ultraminiaturized, implantable optoelectronic technologies; the result provides minimal interruption in natural behaviors and a highly sensitive platform for stable recording of calcium transients in untethered animal models.

The capability for wireless monitoring of cell-type-specific population activity provides advantages over fiber photometry techniques. Possibilities include recording of neuronal activity dynamics during complex behaviors such as those demonstrated in this study and in arenas that would otherwise not allow for neural recordings. During complex behaviors involving multiple animals within a single behavioral session, such as social interaction, sexual behavior, or aggression, fiber photometry presents limitations due to tethers and subjects interacting with the tethers (Movies S1 and S2). The simplicity of the wireless system allows recording of signals from two animals simultaneously without tethers. In addition, the simplicity of the wireless system allows compatibility with behavioral setups that include complex parts (e.g., enriched environment, operant conditioning box, active/passive avoidance, or shuttle box system) and mitigates potential conflicts that may occur between fiber photometry hardware and hardware from sound-attenuated boxes or other wired manipulations (self-administration via catheter injections).

Importantly, the wireless system prevents hindrance of ethologically relevant, naturalistic behaviors in mice that can occur when using a tethered fiber photometry system, thereby reducing confounding effects in acquisition and interpretation of behavioral and neural activity data. Tethered fibers can induce discomfort in the mice and cause behavioral or physiological stress, as well as limit activity during otherwise normal behaviors. The miniaturized designs and low bending stiffness of the injectable probes reduce brain tissue lesioning compared with previously developed in vivo recording methods with chronic deep-brain implantations. In addition, the devices for this technique use straightforward fabrication steps (>90% yields are typical). More than 70% of the implanted wireless photometry probes successfully record Ca^{2+} transient activities inside the brain 6 wk after implantation. Collectively, these and other attractive features of the wireless photometry system introduced here suggest its utility for a wide range of behavioral paradigms and its ready dissemination into the neuroscience research community. Possibilities for extended functional options will follow from integration of multiple μ-ILEDs or fluidic channels on the injectable probe needle to enable wireless optogenetic manipulation (16) or drug delivery (39), along with optical recording. For example, the addition of a red μ-ILED would enable simultaneously optogenetic stimulation with red-shifted channelrhodopsins (40) and Ca^{2+} recording with GCaMP6 from dopaminergic neurons in the ventral tegmental area (VTA), allowing manipulating the response of optogenetic stimulation to match naturalistic VTA dopaminergic reward response.

Materials and Methods

Fabrication of μ-IPDs. Photolithographically defined (AZ nLoF 2070; Integrated Micro Materials) patterns of metal films (Cr/Au, thickness 5 nm/150 nm) deposited by electron-beam evaporation defined the n contacts for μ-IPDs built on an epitaxially grown stack consisting of 0.1-μm Te-doped (1×10^{19} cm^{-3}) n-type GaAs top contact layer, 0.1-μm Si-doped (2×10^{18} cm^{-3}) n-type GaAs top contact layer, 0.025-μm Si-doped (2×10^{18} cm^{-3}) n-type $In_{0.50}Ga_{0.50}P$ window layer, 0.1-μm Si-doped (2×10^{18} cm^{-3}) n-type GaAs emitter layer, 2.5-μm Zn-doped (1×10^{17} cm^{-3}) p-type GaAs base layer, 0.1-μm Zn-doped (5×10^{18} cm^{-3}) p-type $Al_{0.30}Ga_{0.70}As$ BSF layer, and 2-μm Zn-doped (3–5 $\times$ 10^{19} cm^{-3}) p-type GaAs bottom contact layer (*SI Appendix*, Fig. S4). A mixture of H_3PO_4, H_2O_2, and H_2O (3:1:25 by volume) eliminated the Te and Si doped layers. Patterned etching with HCl and H_3PO_4 (1:1 by volume) removed the InGaP window layer. After spin-coating and patterning a photodefinable epoxy (AZ 5214; Microchem) on top of the GaAs wafer, a solution of H_3PO_4, H_2O_2, and H_2O (3:1:25 by volume) selectively removed the Zn-doped GaAs layer. Creating the p contacts for the μ-IPDs followed similar procedures as those described for the n contacts. Immersion in an ethanol-rich HF solution (1.5:1 by volume) eliminated the $Al_{0.95}Ga_{0.05}As$ sacrificial layer, allowing the release of the μ-IPDs from the GaAs wafer.

Fabrication of Wireless Photometry Probes. Fabrication began with lamination of a film of PI (75 μm thick) on a glass slide coated with a layer of PDMS. A flat PDMS stamp enabled transfer printing of individual μ-IPDs from the GaAs wafer to the PI substrate. Spin-casting and patterning a layer of photodefinable epoxy (SU8 2002; Microchem) formed a coating over the device with openings at the p and n contact areas. Photolithography (AZ nLof 2070; Integrated Micro Materials) and lift-off in acetone-defined patterns of Cr/Au/Cu/Au (sputter deposited, thickness ~ 1 μm) for interconnects. A spin-cast layer of a narrow band molecular absorber (ABS 473; Exciton) mixed into a photodefinable epoxy (SU8 2007; Microchem) (1.5 wt %) formed the optical filter (~7 μm thick) on top of the μ-IPD. An In/Ag solder paste (Indalloy 290; Indium Corporation) joined the μ-ILED to the interconnects. Transfer printing placed the Au bond pads of the μ-ILED (C460TR2227-0216; Cree Inc.) onto the paste. Heating at 150 °C for 2 min formed a robust electrical and mechanical bond. Laser-cutting via a UV laser system (LMT-5000 micromachining station; Potomac Photonics, Inc.) defined the shape of the injectable probe. An additional layer of photodefinable epoxy (SU8 2007; Microchem) (thickness ~ 7 μm) acted as an encapsulation layer. Attaching a FFC connector (5034800400; Molex, LLC) to the patterned openings on the interconnects followed steps similar to those for soldering the μ-ILED. A dip-coated layer of PDMS (thickness ~ 10 μm), cured at 70 °C for 2 h, served as a final encapsulation to complete the fabrication. The details appear in *SI Appendix*, Fig. S3.

Fabrication of Transponders. Flexible, copper-clad PI (Pyralux AP 8535R; Dupont) served as the substrate for the wireless transponder circuits. The thickness of the PI and the copper were 75 and 18 μm, respectively. Lamination of the copper-clad substrate to a temporary carrier, namely, a PDMS-coated glass substrate, represented the starting point for the fabrication. A photolithographically patterned layer (SPR 220 7.0; Microchem) served as the etch mask for removal of the copper with a ferric chloride solution (CE-100; Transene). Delamination of the copper-clad PI from the temporary carrier followed by spin coating of PI (PI2545; HD Microsystems) with subsequent cure in a nitrogen atmosphere at 250 °C yielded an encapsulated flexible printed circuit board. Photolithography and reactive ion etching (20 standard-state cubic cm per min O_2; 200 mTorr; 200 W; 1,200 s) defined openings in the PI encapsulation layer to allow electrical connection of the various components of the circuit. A UV laser-cutting tool then defined the outline of the transponder. Low-temperature soldering attached the electrical components to the circuit. *SI Appendix*, Fig. S7 presents a detailed schematic and component description. A 200-μm-thick polyethylene terephthalate layer, bonded to the backside of the circuit by using a rapid-curing 2 component epoxy (5 min Epoxy; Devcon), provided a firm support for the system. The resulting thickness of the circuit matched the requirements for use of the FFC connector. Bonding and electronically connecting a lightweight (0.33 g), 12-mAh rechargeable battery (GMB-300910; Guangzhou Markyn Battery Co., Ltd.) followed procedures similar to those for attaching the FFC connector.

Electrical Component Choice and Programming. The requirements for small size and lightweight construction necessitated careful selection of the electrical components. Small-outline passive components (0201 standard), ball grid-mounted analog (ADA4505-2 1.42 × 1.42 mm; Analog Devices), and small-outline μC (AtTiny84 4 mm × 4 mm; Atmel) were selected. The software consisted of two distinct pieces of code: the wireless transponder and the receiver. The wireless transponder software featured control over the fluorescence stimulating μ-ILED and the digitalization of the amplified μ-IPD signal, the encoding of the signal into the NEC code, the modulating of the signal onto a 38-kHz carrier frequency, and the transmission of the signal via the IR LED (Kingbright 940 nm 120° 0402 standard). The receiver software featured decoding of the signal as well as time stamping and interfacing to a personal computer. The complete program flow is in *SI Appendix*, Fig. S18.

Optical Simulations. Details of optical simulations appear in *SI Appendix*, Note S1.

Fiber Photometry System. A 470-nm LED operating at 211 Hz served as the light source for fiber photometry system. The light passed through a green fluorescent protein (GFP) excitation filter, coupled to a high-NA (0.48), large-core (400 μm) optical fiber patch cord, and a 0.48-NA, 400-μm fiber-optic implant in each mouse. The optical fiber first collected GCaMP6f fluorescence, which then passed through a GFP emission filter and focused onto a photoreceiver (Newport 2151; Doric Lenses Inc.). Software running on a real-time signal processor (Synapse, RZ5P; Tucker Davis Tech.) controlled the LED and demodulated the incoming signal.

Experimental Animals. All experiments used adult male WT C57BL/6 mice (9–12 wk old at start of experiments). Mice (25–35 g at the start of testing) were maintained on a 12-h light/dark cycle (lights on at 7:00 AM) and given access to food and water ad libitum. Mice were group-housed (three to five per cage) before wireless or fiber photometry probe implantation, after which mice were individually housed. Mice were held in a climate-controlled facility adjacent to the rooms for behavioral tests. All procedures agree with the National Institutes of Health standards and were approved by the Animal Care and Use Committee of Washington University in Saint Louis.

Stereotaxic Surgery. Mice were anesthetized in an induction chamber (4% isoflurane) and then placed in a stereotaxic frame where they were maintained at 1–2% isoflurane. Incisions were made to expose the skull, and three burr holes were drilled both above the viral injection site and for the placement of two anchor screws. Mice were injected with AAVDJ-CaMKIIα-GCaMP6f (1.31×10^{13} viral genomes/mL; UPENN; diluted to 1:3) into the BLA [anterior–posterior (AP), −1.9; medial–lateral (ML), +3.2; dorsal–ventral (DV), −4.6]. Allowing for viral expression to incur, 1–2 wk after injection, mice were then implanted with either the wireless or fiber photometry probes in the BLA (wireless probe: AP, −1.6; ML, +3.35; DV, −5.6; and fiber probe: AP, −1.6; ML, +3; DV, −4.6). The device was then slowly lowered into the BLA with a stable stereotaxic holder. Photometry probes and anchor screws were then affixed to the skull by using both super glue and dental cement. *SI Appendix*, Fig. S19 shows the images of the surgery. Mice recovered for at least 1 wk before any testing.

Immunohistochemistry. Immunohistochemistry was performed as described by Siuda et al. and Jeong et al. (36, 39). Mice were given a lethal dose of pentobarbital sodium and intracardially perfused with 4% paraformaldehyde in PBS. Brains were dissected, postfixed for 24 h at 4 °C, and cryoprotected with a solution of 30% sucrose in 0.1 M phosphate buffer (pH 7.4) at 4 °C for at least 24 h. Brains were then cut into 30-μm sections. Thirty-micrometer brain sections were washed two or three times in PBS and blocked in blocking buffer (PBS containing 0.5% Triton X-100 and 5% normal goat serum) for 1 h. Sections were then incubated for ∼16 h at 4 °C in blocking buffer containing guinea pig anti-GFAP (1:500) and rabbit anti-Iba1 (1:300). Following incubation, sections were washed three times in PBS and then incubated for 2 h at room temperature in blocking buffer containing Alexa Fluor 633 goat anti-rabbit IgG (1:1,000), Alexa Fluor 546 goat anti-guinea pig IgG (1:1,000), and Neurotrace 435/455 Blue Fluorescent Nissl stain (1:400). Following the secondary antibody, sections were washed three times in PBS followed by three washes in phosphate buffer and then mounted on glass slides with hardset Vectashield (Vector Labs; *SI Appendix*, Table S3). All sections were imaged on a confocal microscope. Gain, exposure time, and z-stack size remained constant throughout each experiment. All images were processed with the same settings by using Fiji ImageJ.

Immuno-Glial Response in Implanted Tissues. C57BL/6J mice ($n = 3$ per group) were implanted with fiber or wireless photometry probes into the BLA and allowed to recover for 4 wk before perfusion. Immunohistochemistry was performed as described above.

Behavioral Experiments. All behavioral experiments were performed during the light phase (7:00 AM–7:00 PM) in sound-attenuated rooms maintained at 23 °C. For fiber photometry, a fiber-optic patch cord (400 μm, 0.48 NA; Doric Lenses Inc.) was connected to the implanted optical fiber (400 μm, MF2.5; Doric Lenses Inc.) during testing. For wireless photometry, the transponder was connected to the wireless probes before the testing. Mice were handled days before behavioral tests to acclimate the subjects to the experimenter and reduce the stress response. Fiber photometry mice were habituated to the fiber photometry tethering for 3 d before behavioral tests in a home cage. Immediately before all rodent tests, animals were habituated in the behavior testing room for at least 30 min. Animals undergoing neural recording experiments were killed, and fiber-optic or wireless photometry probe placements in the brain were checked. Animals with placements of the probe outside of the region of interest were excluded from analysis.

Foot-Shock Tests. Mice received foot shocks in chambers that are typically used for fear conditioning. The chambers (30 cm wide, 24 cm deep, and 22 cm high; Med Associates) consisted of a rectangular arena with floors made of stainless steel rods (2 mm diameter, spaced 5 mm apart) and walls of aluminum and acrylic. Mice were placed in the foot-shock chamber, habituated for 2 min, and given five electrical foot shocks (0.7 mA, 1 s) signaled from a shock generator (ENV-410B; Med Associates) every 2 min. The chamber was cleaned with 70% ethanol between runs. Baseline photometric recordings were taken during the two first minutes of habituation and every 2 min in between foot shock therein.

Beta-Adrenergic Receptor Agonist Stimulated BLA Calcium Transient Detection. Mice were hooked up to the photometry systems (wireless or fiber) and allowed to acclimate with the devices for 5–10 min in their home cage. Baseline recordings of 10 min were taken before drug administration. Mice were then administered isoproterenol (4 mg/kg, i.p.; Sigma Aldrich), a selective β-adrenoreceptor agonist. Immediately after injection, mice were placed back in their home cage. Mice stayed in their home cage for neural activity recordings for 50 min after drug injection. The data of each mouse were normalized with its own baseline. Mice injected with saline and fiber-based photometry systems served as references for comparison. The event detection method used was identical to the foot-shock test. All mice were pseudorandomly assigned by the experimenter to either drug or vehicle treatments in a counterbalanced fashion within each cage and day of experiment. One week later, the same mice were tested in the opposing condition to assess the data in both within- and between-subjects manners.

OFT. OFT was performed in a 2,500-cm^2 square arena. Lighting was measured and stabilized at ∼400 lx. The arena was cleaned with 70% ethanol between testing trials. Fiber photometry mice were habituated to the fiber photometry tethering for 3 d before behavioral tests in a home cage. Wireless-implanted mice were similarly handled for a few days before testing. For testing, C57Bl6 mice either implanted with fiber or wireless photometry probes ($n = 8$ or 9 per group) were placed in the center of the open field and allowed to roam freely for 20 min. Movements were video-recorded and analyzed by using Ethovision 11. The center was defined as a square comprising 50% of the total area of the OFT. Time in the center was the primary measure of anxiety-like behaviors. All animals were pseudorandomly assigned to position in the behavioral cohort by the experimenter. However, the experimenter was not blind to treatment due to the visible device. Computerized analysis allowed for blind analysis.

Rotarod Assay. An accelerating rotarod (Ugo Basile) was used to assess motor coordination of C57Bl6 mice implanted with either fiber or wireless photometry probes ($n = 5$ per group) received two training sessions separated by 1 h. The first training session consisted of two trials of 120 s spent walking on the rotarod at a fixed speed of 4 rpm. The second training session consisted of one trial of 120 s at 4 rpm. All mice completed the first training session without falling in five attempts or less. All mice completed the second training session in two attempts or less without a fall. One hour after the second training session, latency to fall as the rotarod accelerated from 4 to 40 rpm over 5 min was assessed. Five consecutive acceleration trials were performed, with 10 min between each trial. All animals were pseudorandomly assigned to position in behavioral cohort by the experimenter. However, the experimenter was not blind to treatment due to the visible device. Computerized analysis allowed for blind analysis.

Social Interaction Assay. Social interaction was performed in a 27-cm^2 chamber. C57Bl6 mice implanted with either fiber or wireless photometry probes ($n = 8$ or 9 per group) could explore freely for 5 min (habituation). A naive, novel age-, strain-, and weight-matched conspecific was then introduced to the chamber and allowed to explore freely for an additional 5 min (test session). All behaviors were recorded by using Ethovision 11 and manually scored and analyzed by a blind experimenter using behavioral analysis software (JWatcher). The overall score of social interaction included behaviors such as head, body, and anogenital sniffing, and direct contact.

Data Collection and Statistical Analysis. A 470-nm LED was modulated at 211 Hz and passed through a 470-nm bandpass filter. The fiber fluorescence signal was collected with an acquisition rate 1,017 Hz as the amplified photovoltage from the photoreceiver via Synapse software (TDT), "locked in," and demodulated by using the software's fiber photometry gizmo. Excitation light at 470 nm passed through a fluorescence mini cube (Doric Lenses). The fluorescence emitted by the GCaMP6f was detected in the 528- to 556-nm window of the device, which was then delivered through the TDT RZ5P Processor for data acquisition. Acquired data files were then extracted by using Matlab and downsampled to match the rate of the wireless device. In some recording sessions, there was a signal decay observed after the pharmacological injection. To address this in a general way, we used a Butterworth digital high-pass (0.1 Hz) filter to collect the baseline. After the baseline correction, the signal was transferred into $\Delta F/F_0$ by

$$\Delta F/F_0 = \frac{F(t) - F(0)}{F(0)} \quad [1]$$

Change of frequency was calculated by:

$$\frac{\Delta \text{events}}{\text{minute}} = \frac{\text{events}}{\text{minute post injection}} - \frac{\text{events}}{\text{minute baseline}} \quad [2]$$

The SNR was calculated by:

$$\text{SNR} = \frac{\max(\text{peaks})}{s.d.(\text{baseline})} \quad [3]$$

The threshold was set up as the median absolute deviation (MAD) of the baseline, and all of the local maximum values $>5 \times$ MAD were defined as neuronal activity events. All negative events were discarded.

$$\text{MAD} = \text{median}_i\left(\left|X_i - \text{median}_j\left(X_j\right)\right|\right) \quad [4]$$

Data were expressed as means ± SEM. Data were normally distributed, and differences between groups were determined by using independent *t* tests or one- or two-way ANOVA followed by post hoc Bonferroni comparisons if the main effect was significant at $P < 0.05$. Paired *t* tests were used in within-subject design experiments. Prism (Version 7.0; GraphPad), Matlab (Version R2015a), and Python (Version 2.7) were used for all data analysis, computation, and statistical comparisons. For all behavioral studies during neural recording, 7–10 animals for each photometry probe were chosen since a sample size of 8 in each group would have 99% power to detect this difference in means, assuming a SD of 0.75 using a two-group *t* test with a 0.05 two-sided significance level. Column statistics were used to determine a normal distribution between the groups, and D'Agostino and Pearson omnibus normality tests were used to determine if our subject number was sufficient. Furthermore, we used a within-subjects design to appropriately compare neural activity during vehicle or treatment.

Code Availability. Code used for operation and analysis in this study is freely available on GitHub (https://github.com/PhilippGutruf/Wireless-implantable-optoelectronic-photometers-for-monitoring-neuronal-dynamics-in-the-deep-brain).

ACKNOWLEDGMENTS. This work was supported by NIH BRAIN Initiative Grant R21EY027612A (to M.R.B. and J.A.R.) and National Institute of Mental Health Grant R01MH112355 (to M.R.B.). X. Sheng was supported by National Natural Science Foundation of China Project 51602172. A.V.-G. and D.C. were supported Northrop Grumman Corp. Grant 63018088.

1. Zhao Y, et al. (2011) An expanded palette of genetically encoded Ca^{2+} indicators. *Science* 333:1888–1891.
2. Akerboom J, et al. (2012) Optimization of a GCaMP calcium indicator for neural activity imaging. *J Neurosci* 32:13819–13840.
3. Chen T-W, et al. (2013) Ultrasensitive fluorescent proteins for imaging neuronal activity. *Nature* 499:295–300.
4. Ghosh KK, et al. (2011) Miniaturized integration of a fluorescence microscope. *Nat Methods* 8:871–878.
5. Flusberg BA, et al. (2008) High-speed, miniaturized fluorescence microscopy in freely moving mice. *Nat Methods* 5:935–938.
6. Cui G, et al. (2013) Concurrent activation of striatal direct and indirect pathways during action initiation. *Nature* 494:238–242.
7. Gunaydin LA, et al. (2014) Natural neural projection dynamics underlying social behavior. *Cell* 157:1535–1551.
8. Jennings JH, et al. (2015) Visualizing hypothalamic network dynamics for appetitive and consummatory behaviors. *Cell* 160:516–527.
9. Grewe BF, et al. (2017) Neural ensemble dynamics underlying a long-term associative memory. *Nature* 543:670–675.
10. Yu H, Senarathna J, Tyler BM, Thakor NV, Pathak AP (2015) Miniaturized optical neuroimaging in unrestrained animals. *Neuroimage* 113:397–406.
11. Miao P, et al. (2016) Chronic wide-field imaging of brain hemodynamics in behaving animals. *Biomed Opt Express* 8:436–445.
12. Sigal I, et al. (2016) Imaging brain activity during seizures in freely behaving rats using a miniature multi-modal imaging system. *Biomed Opt Express* 7:3596–3609.
13. Gilletti A, Muthuswamy J (2006) Brain micromotion around implants in the rodent somatosensory cortex. *J Neural Eng* 3:189–195.
14. Sridharan A, Rajan SD, Muthuswamy J (2013) Long-term changes in the material properties of brain tissue at the implant-tissue interface. *J Neural Eng* 10:066001.
15. Yoon J, et al. (2010) GaAs photovoltaics and optoelectronics using releasable multilayer epitaxial assemblies. *Nature* 465:329–333.
16. Park SI, et al. (2015) Soft, stretchable, fully implantable miniaturized optoelectronic systems for wireless optogenetics. *Nat Biotechnol* 33:1280–1286.
17. Kim TI, et al. (2013) Injectable, cellular-scale optoelectronics with applications for wireless optogenetics. *Science* 340:211–216.
18. Kim CK, et al. (2016) Simultaneous fast measurement of circuit dynamics at multiple sites across the mammalian brain. *Nat Methods* 13:325–328.
19. Cui G, et al. (2014) Deep brain optical measurements of cell type-specific neural activity in behaving mice. *Nat Protoc* 9:1213–1228.
20. Soares S, Atallah BV, Paton JJ (2016) Midbrain dopamine neurons control judgment of time. *Science* 354:1273–1277.
21. Kim D-H, et al. (2010) Dissolvable films of silk fibroin for ultrathin conformal bio-integrated electronics. *Nat Mater* 9:511–517.
22. Luan L, et al. (2017) Ultraflexible nanoelectronic probes form reliable, glial scar-free neural integration. *Sci Adv* 3:e1601966.
23. Badura A, Sun XR, Giovannucci A, Lynch LA, Wang SSH (2014) Fast calcium sensor proteins for monitoring neural activity. *Neurophotonics* 1:025008.
24. Shin G, et al. (2017) Flexible near-field wireless optoelectronics as subdermal implants for broad applications in optogenetics. *Neuron* 93:509–521.e3.
25. Stujenske JM, Spellman T, Gordon JA (2015) Modeling the spatiotemporal dynamics of light and heat propagation for in vivo optogenetics. *Cell Rep* 12:525–534.
26. Grienberger C, Konnerth A (2012) Imaging calcium in neurons. *Neuron* 73:862–885.
27. Richards PL (1994) Bolometers for infrared and millimeter waves. *J Appl Phys* 76:1–24.
28. Yaroslavsky AN, et al. (2002) Optical properties of selected native and coagulated human brain tissues in vitro in the visible and near infrared spectral range. *Phys Med Biol* 47:2059–2073.
29. Yona G, Meitav N, Kahn I, Shoham S (2016) Realistic numerical and analytical modeling of light scattering in brain tissue for optogenetic applications. *eNeuro* 3: ENEURO.0059-15.2015.
30. Al-Juboori SI, et al. (2013) Light scattering properties vary across different regions of the adult mouse brain. *PLoS One* 8:e67626.
31. Yizhar O, Fenno LE, Davidson TJ, Mogri M, Deisseroth K (2011) Optogenetics in neural systems. *Neuron* 71:9–34.
32. Dombeck DA, Khabbaz AN, Collman F, Adelman TL, Tank DW (2007) Imaging large-scale neural activity with cellular resolution in awake, mobile mice. *Neuron* 56:43–57.
33. Grewe BF, Langer D, Kasper H, Kampa BM, Helmchen F (2010) High-speed in vivo calcium imaging reveals neuronal network activity with near-millisecond precision. *Nat Methods* 7:399–405.
34. Tye KM, et al. (2011) Amygdala circuitry mediating reversible and bidirectional control of anxiety. *Nature* 471:358–362.
35. Siuda ER, et al. (2015) Optodynamic simulation of β-adrenergic receptor signalling. *Nat Commun* 6:8480.
36. Siuda ER, Al-Hasani R, McCall JG, Bhatti DL, Bruchas MR (2016) Chemogenetic and optogenetic activation of Gαs signaling in the basolateral amygdala induces acute and social anxiety-like states. *Neuropsychopharmacology* 41:2011–2023.
37. Bush DE, Caparosa EM, Gekker A, Ledoux J (2010) Beta-adrenergic receptors in the lateral nucleus of the amygdala contribute to the acquisition but not the consolidation of auditory fear conditioning. *Front Behav Neurosci* 4:154.
38. Grillon C, Cordova J, Morgan CA, Charney DS, Davis M (2004) Effects of the beta-blocker propranolol on cued and contextual fear conditioning in humans. *Psychopharmacology (Berl)* 175:342–352.
39. Jeong J-W, et al. (2015) Wireless optofluidic systems for programmable in vivo pharmacology and optogenetics. *Cell* 162:662–674.
40. Rajasethupathy P, et al. (2015) Projections from neocortex mediate top-down control of memory retrieval. *Nature* 526:653–659.

Wireless optoelectronic photometers for monitoring neuronal dynamics in the deep brain

Luyao Lu[a,b,1], Philipp Gutruf[a,b,1], Li Xia[c,1], Dionnet L. Bhatti[d,e,1], Xinying Wang[f], Abraham Vazquez-Guardado[g,h], Xin Ning[a], Xinru Shen[a], Tian Sang[a], Rongxue Ma[a], Grace Pakeltis[a], Gabriel Sobczak[c], Hao Zhang[b], Dong-oh Seo[d,e], Mantian Xue[a], Lan Yin[i], Debashis Chanda[g,h], Xing Sheng[j,2], Michael R. Bruchas[c,d,e,k,l,2], and John A. Rogers[a,b,m,n,o,p,q,r,s,t,2]

[a]Department of Materials Science and Engineering, Frederick Seitz Materials Research Laboratory, University of Illinois at Urbana-Champaign, Urbana, IL 61801; [b]Department of Materials Science and Engineering, Northwestern University, Evanston, IL 60208; [c]Department of Biomedical Engineering, Washington University School of Medicine, St. Louis, *MO* 63130; [d]Washington University Pain Center, Washington University School of Medicine, St. Louis, *MO* 63130; [e]Department of Anesthesiology, Washington University School of Medicine, St. Louis, *MO* 63130; [f]Department of Electrical and Computer Engineering, University of Illinois at Urbana-Champaign, Urbana, IL 61801; [g]CREOL, The College of Optics and Photonics, University of Central Florida, Orlando, FL 32816; [h]NanoScience Technology Center, University of Central Florida, Orlando, FL 32826; [i]School of Materials Science and Engineering, Tsinghua University, Beijing, 100084; [j]Department of Electronic Engineering, Tsinghua University, Beijing, 100084; [k]Department of Neuroscience, Washington University School of Medicine, St. Louis, *MO* 63110; [l]Division of Biology and Biomedical Sciences, Washington University School of Medicine, St. Louis, *MO* 63110; [m]Department of Biomedical Engineering, Northwestern University, Evanston, IL 60208; [n]Department of Chemistry, Northwestern University, Evanston, IL 60208; [o]Department of Mechanical Engineering, Northwestern University, Evanston, IL 60208; [p]Department of Electrical Engineering and Computer Science, Northwestern University, Evanston, IL 60208; [q]Simpson Querrey Institute, Northwestern University, Evanston, IL 60208; [r]Feinberg School of Medicine, Northwestern University, Evanston, IL 60208; [s]Department of Neurological Surgery, Northwestern University, Evanston, IL 60208; and [t]Center for Bio-Integrated Electronics, Northwestern University, Evanston, IL 60208

[1]These authors contributed equally to this work.

[2]To whom correspondence should be addressed. Email: jrogers@northwestern.edu or bruchasm@wustl.edu or xingsheng@tsinghua.edu.cn.

List of contents:

Supplementary Note 1: Optical Simulations. Ray tracing was conducted using a custom MATLAB script, which uniformly discretizes the illumination volume (*dx*, *dy* and *dz* = 5 μm), sweeps the polar and azimuthal angles representing the possible direction of fluorescence emission, and calculates the corresponding solid angle that lands on the of the detector's area. The modeled brain tissue (adult male cortex) is optically dense (n_B = 1.36), with absorption coefficient α_0 = 0.6 cm^{-1}, scattering coefficient α_s = 211 cm^{-1} and anisotropy factor *g* = 0.86 (primarily forward scattering) (1, 2). In addition, the modeled brain tissue is assumed to be uniformly labeled with molar absorptivity of 5.03 x 10^4 $cm^{-1}M^{-1}$. The assumed GCaMP6 concentration is 500 μM, corresponding to an absorption coefficient α_d of 25 cm^{-1}. Hence, the total absorption coefficient becomes $\alpha_T = \alpha_0 + \alpha_d$ = 25.6 cm^{-1}, mostly dominated by GCaMP6 absorption. Considering all such loss channels, the effective absorption, derived by the Radiative Transfer Equation under predominantly forward scattering and steady state operation, is

$$\alpha_{eff} = \sqrt{3\alpha_T(\alpha_T + \alpha_s(1-g))} \quad (1)$$

The wireless photometry system model consists of an emulated brain tissue superstrate, as previously described, and PDMS (n_{PDMS} = 1.4) that encapsulates both the μ-ILED and μ-IPD. The modeled μ-ILED emission profile, $I_{em}(r,z)$, where $r = (x,y)$, consisted on a normalized Gaussian intensity distribution that propagates in the superstrate with width waist $2w_{0x}$ and $2w_{0y}$ of 270 μm and 220 μm (μ-ILED footprint), as shown below:

$$I_{em}(r,z) = I_0 \frac{w_{0x}w_{0y}}{w_x(z)w_y(z)} e^{-\frac{2x^2}{w_x^2(z)}\frac{2y^2}{w_y^2(z)}} e^{-\alpha_{eff}z} \quad (2)$$

The μ-ILED has 70º full divergence angle (NA = 0.78), producing beam divergence as $w_x(z) \approx w_{0x} + z\tan(35º)$ and $w_y(z) \approx w_{0y} + z\tan(35º)$. This divergence angle is determined by the critical emission angle of the μ-ILED in the PDMS/brain tissue.

The μ-ILED emission profile produces a total illumination volume of 5.3 x 10^7 μm^3 in the emulated brain tissue. GCaMP6 absorbs the μ-ILED light in this volume and, in turn, emits isotropically with

a quantum efficiency (*QE*) of ~67%, $I_f(r,z) = I_{em}(r,z)*QE$, whose fluorescence volume is 4.0 x 10^7 μm^3. On the other hand, the μ-IPD captures photons within a solid angle determined by the detector area and point of sight. The normalized solid angle volume distribution $\vartheta(r,z)$ is given by:

$$\vartheta(r,z) = \frac{1}{4\pi}\int_{\theta_l}^{\theta_H}\int_{\theta_l}^{\theta_H} \sin\theta_r \, d\theta_r \, d\emptyset_r \quad (3)$$

where θ_r is the polar angle (0 - π/2) and ϕ_r is the azimuthal angle (0 - 2π). Furthermore, the μ-IPD has an acceptance angle of 85º and a NA of 1.35.

Same methodology is followed for the optics associated with the fiber systems. The emission light couples out of the fiber and propagates in the modeled brain tissue, as described above, with a full divergence angle of 42º, determined by the numerical aperture of the fiber (0.48): $NA = n_B \sin(\theta)$. The fluorescence emission profile was modeled as a Gaussian intensity distribution with width waist of $2w_0$ of 400 μm and divergence determined by $w(z) \approx w_0 + z \tan(21º)$, as shown below:

$$I_f(r,z) = I_0 QE \frac{w_0^2}{w^2(z)} e^{-\frac{2\rho^2}{w^2(z)}} e^{-\alpha_{eff} z} \quad (4)$$

where $\rho^2 = x^2 + y^2$ and α_{eff} is the effective absorption, as previously described. The corresponding illumination and fluorescence volumes for these particular fiber parameters are 1.2 x 10^8 μm^3 and 9.8 x 10^7 μm^3, respectively. Finally, the angular capture efficiency $\vartheta(r,z)$ was calculated in the same way using equation (3) but only varying the azimuthal angle within the NA of the fiber (±21º). Volume integration for both systems was carried out within the boundary where the parameters (illumination, fluorescence, and angular capture efficiency) are larger than 1% of initial values.

Reference

1. Yaroslavsky AN, et al. (2002) Optical properties of selected native and coagulated human brain tissues in vitro in the visible and near infrared spectral range. *Phys Med Biol* 47:2059-2073.

2. Yona G, Meitav N, Kahn I, Shoham S (2016) Realistic numerical and analytical modeling of light scattering in brain tissue for optogenetic applications. *eNeuro* 3:ENEURO.0059-0015.2015.

Supplementary Figure Legends

Supplementary Fig. 1: Colorized SEM image of a photometer needle with a tilted view. Scale bar, 200 μm.

Supplementary Fig. 2: Schematic illustration of an intact photometer probe.

Supplementary Fig. 3: Schematic illustration of fabrication steps for the photometer probe. (A) Transfer print a μ-IPD onto a 75 μm thick PI substrate. (B) Pattern metal interconnects. (C) Pattern 7 μm thick absorber layer on top of the μ-IPD. (D) Transfer print and solder a μ-ILED on the PI substrate. (E) Define the needle structure by laser cutting. (F) Encapsulate the injectable needle with PDMS.

Supplementary Fig. 4: Schematic illustration of the GaAs photodetector stack design.

Supplementary Fig. 5: Image of an optical cannula on a fingertip. Scale bar, 12 mm.

Supplementary Fig. 6: Weight of the wireless photometry system (A), a 3-D printed transparent head protector (B), a cannula (C), and a patch cord with cannula (D) for fiber photometry system.

Supplementary Fig. 7: Circuit design for wireless photometry transponder and injectable.

Supplementary Fig. 8: (A) Photograph of a wired photometry system next to a US quarter. Scale bar, 6 mm. (B) Photograph of a moving mouse during recording. Scale bar, 1.2 cm. (C) *In vitro* measurement of fluorescence intensity changes with different Ca^{2+} concentrations from 0.1 μM to 50 μM by the wired photometry probe. (D) Electronic working principle of the wired photometry system.

Supplementary Fig. 9: Current-voltage characterizations of μ-IPD and μ-ILED. (A) Current density versus voltage curve of a representative μ-IPD under AM 1.5 G illumination at 100 mW/cm^2. (B) Current versus voltage curve of a representative μ-ILED.

Supplementary Fig. 10: Normalized emission spectrum of an operating μ-ILED on the injectable needle.

Supplementary Fig. 11: Normalized photovoltage signals from the μ-IPD at ambient condition versus function time after immersion in phosphate-buffered saline with temperatures of 90 °C, 75 °C, and 37 °C.

Supplementary Fig. 12: Image of a wireless photometry system operating after implanted in BLA region for 2 months. Scale bar, 2 mm.

Supplementary Fig. 13: Graph displaying data rates in a 60 cm x 60 cm test cage with an opaque enclosure in the center. Receiver location is marked in orange. Data rates are recorded in Hz, counting only successful 12 bit data package transmissions, with a transponder facing in all cardinal directions. Transponder facing north (I); transponder facing east (II); transponder facing south (III); transponder facing west (IV).

Supplementary Fig. 14: (A) Wireless receiver station with quad receiver modules. Scale bar, 5 cm. (B) Opened housing for social animal interaction recording. Scale bar, 1 cm. (C) Image of the fiber photometry system next to a home cage. Scale bar, 15 cm.

Supplementary Fig. 15: (A) Fluorescence spectrum of 0.3 μM Oregon Green® 488 BAPTA-2 calcium indicator mixed with 0.1 μM $CaCl_2$, excited at 488 nm. (B) Fluorescence spectrum of a 75 μm thick PI film excited at 488 nm.

Supplementary Fig. 16: (A) Normalized emission intensity profile with 1% contour for the optical fiber as a function of depth in brain tissue. (Inset) Emission intensity at positions 5 μm and 50 μm above the optical fiber. (B) Spatial distribution of fluorescence intensity captured at the tip of the optical fiber as a function of depth in brain tissue. (Inset) Fluorescence intensity at positions 5 μm and 50 μm above the tip of the optical fiber.

Supplementary Fig. 17: Wireless photometry systems for neural recordings in freely-behaving animals. (A) Tethered fiber-implanted and tetherless wireless-implanted mice do not differ in the amount of time immobile in the OFT. (B) Wireless-implanted mice have increased velocity during the OFT (2-tailed test, *$p<0.05$, $n=7$-9). (C) Photograph of wireless-implanted mouse

performing the rotarod task. Scale bar, 1 cm. (D) Chronic implantation of the wireless devices does not alter motor coordination in a rotarod assay (n=8-10/group, 2-way ANOVA, p=.16). (E) Overlay of lesion areas resulting from chronic implantation (wireless =blue; fiber=grey). (F-G) Photograph of mouse, (F) tethered and implanted with a traditional fiber optic probe or (G) attached to the complete wireless photometry probe. Scale bars, 1 cm. (H) Confocal image of lesion at the site of recording showing expression of calcium indicator GCaMP6f around the site of the wireless photometry probe. Scale bar, 75 μm.

Supplementary Fig. 18: Program flow for wireless transponder and receiver.

Supplementary Fig. 19: Surgery process. (A) The anesthetized mouse is head-fixed on the stereotax. (B) Fur is razed and skin is cut and opened with scalpel. (C) A hole is opened with a drill bit for probe implant, and a screw is driven into the other side of skull as support. (D) Device is delivered by a holder upon the hole. (E) Slowly low down the probe until get BLA region set by the coordinates. (F) Superglue is used to attach the device, skull and the supportive screw. Then dental cement is applied to build up a cup for further securing and protection. Scale bar, 13 mm.

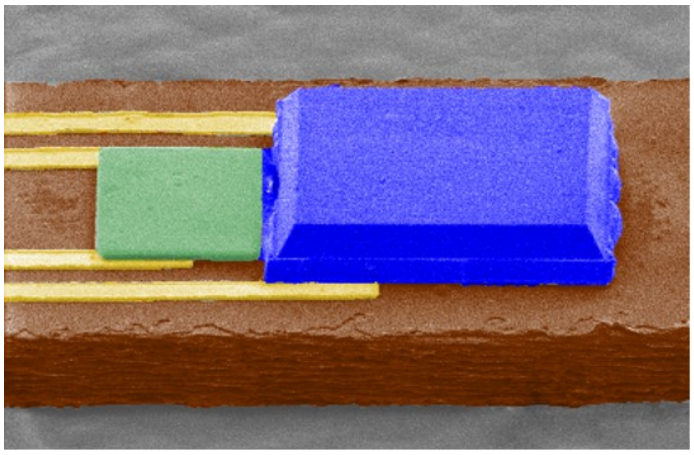

Supplementary Fig. 1: Colorized SEM image of a photometer needle with a tilted view. Scale bar, 200 μm.

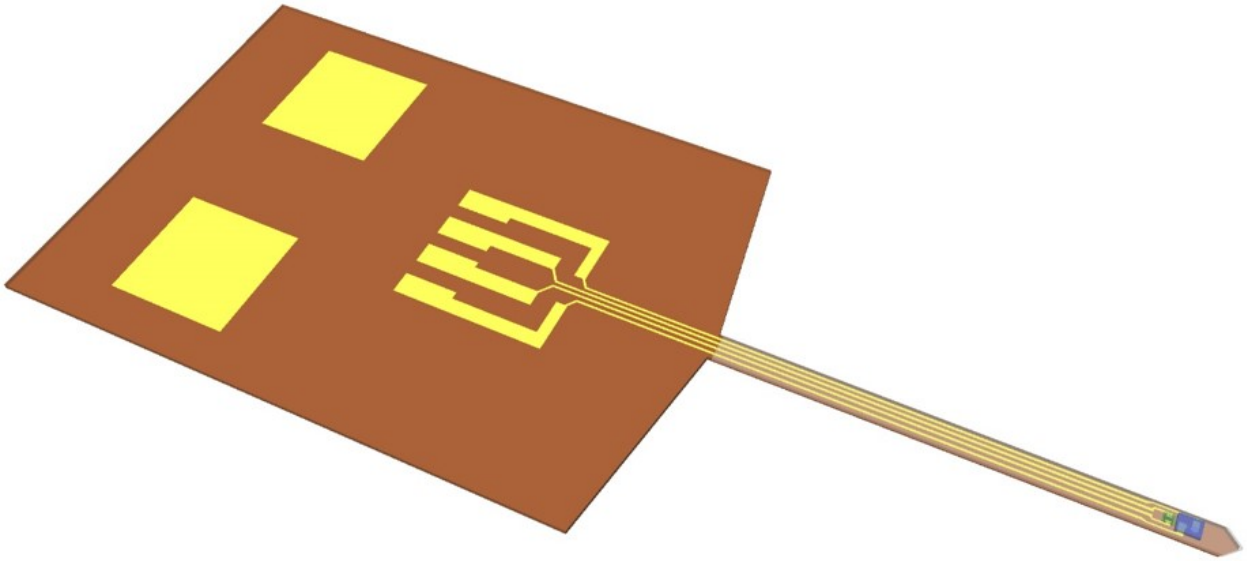

Supplementary Fig. 2: Schematic illustration of an intact photometer probe.

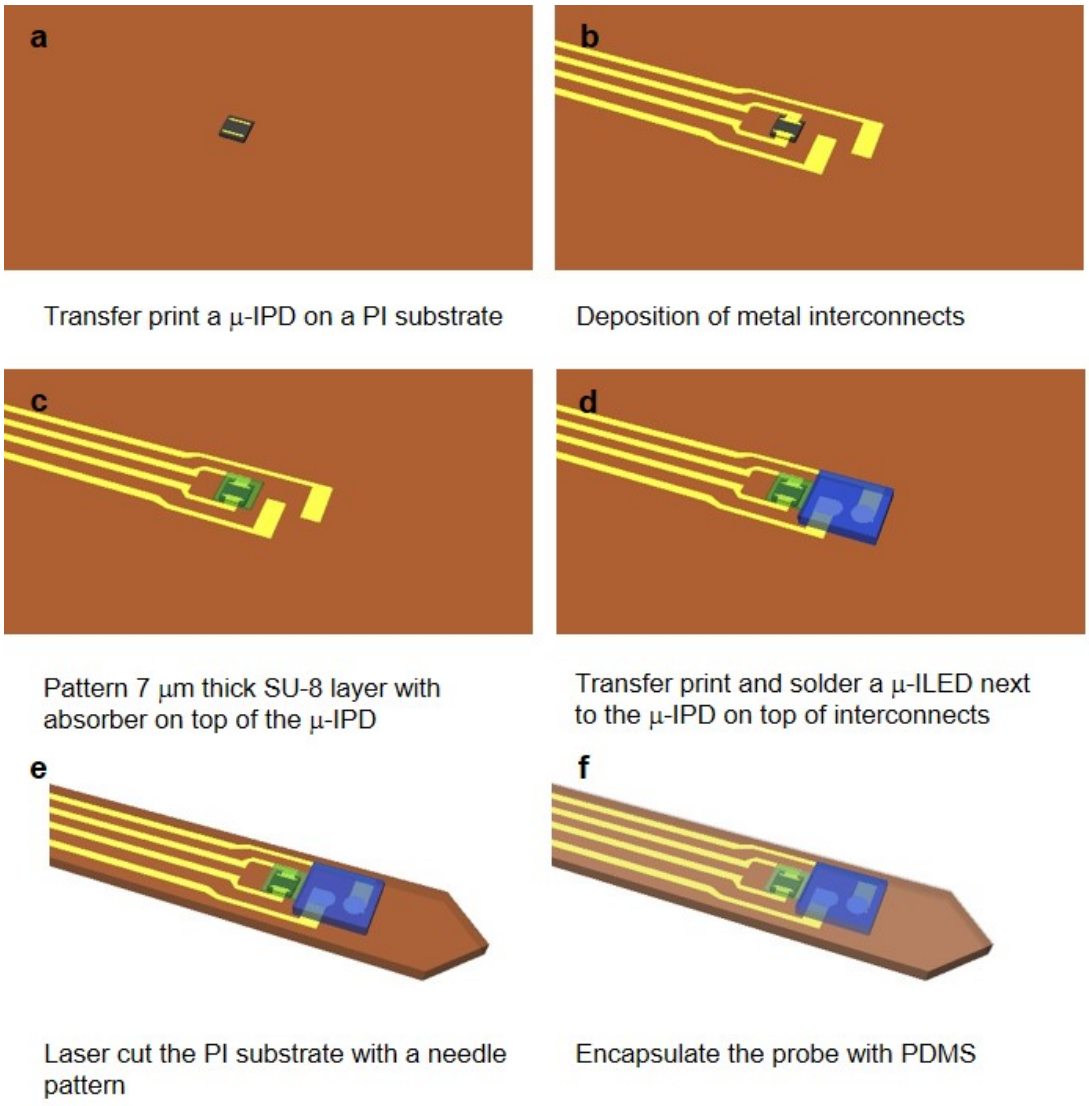

Supplementary Fig. 3: Schematic illustration of fabrication steps for the photometer probe. (A) Transfer print a μ-IPD onto a 75 μm thick PI substrate. (B) Pattern metal interconnects. (C) Pattern 7 μm thick absorber layer on top of the μ-IPD. (D) Transfer print and solder a μ-ILED on the PI substrate. (E) Define the needle structure by laser cutting. (F) Encapsulate the injectable needle with PDMS.

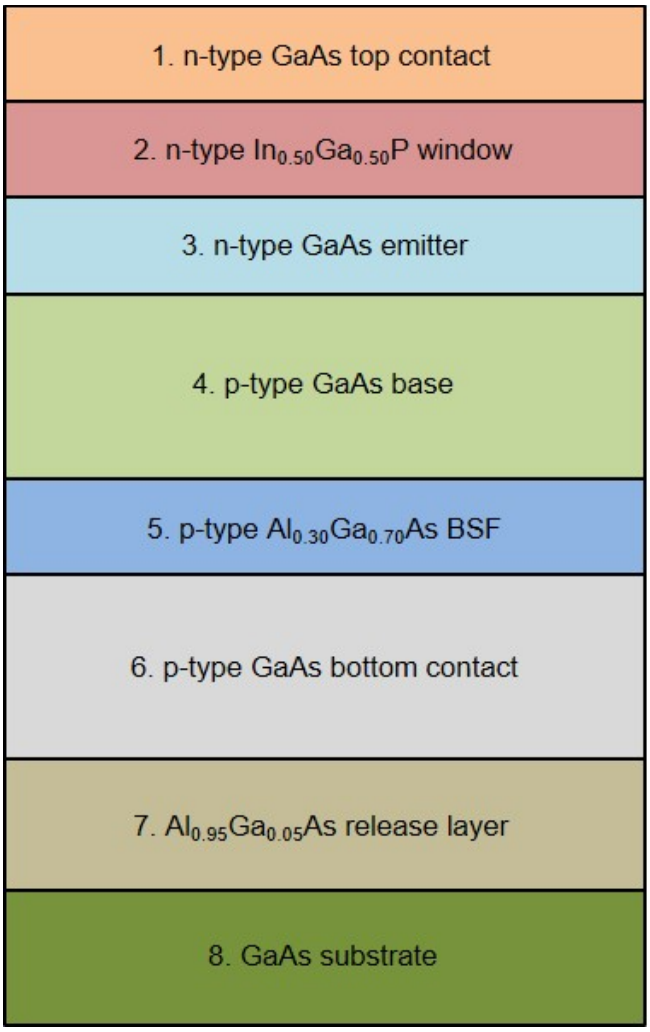

1. n-type GaAs top contact layer
   0.1 μm, Te-doped, $1x10^{19}$ cm^{-3}
   0.1 μm, Si-doped, $2x10^{18}$ cm^{-3}
2. n-type $In_{0.50}Ga_{0.50}P$ window layer
   0.025 μm, Si-doped, $2x10^{18}$ cm^{-3}
3. n-type GaAs emitter layer
   0.1 μm, Si-doped, $2x10^{18}$ cm^{-3}
4. p-type GaAs base layer
   2.5 μm, Zn-doped, $1x10^{17}$ cm^{-3}
5. p-type $Al_{0.30}Ga_{0.70}As$ BSF layer
   0.1 μm, Zn-doped, $5x10^{18}$ cm^{-3}
6. p-type GaAs bottom contact layer
   2 μm, Zn-doped, 3-$5x10^{19}$ cm^{-3}
7. $Al_{0.95}Ga_{0.05}As$ release layer
   0.5 μm
8. GaAs substrate

Supplementary Fig. 4: Schematic illustration of the GaAs photodetector stack design.

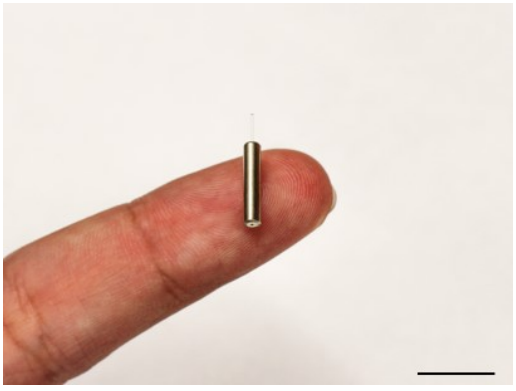

Supplementary Fig. 5: Image of an optical cannula on a fingertip. Scale bar, 12 mm.

Supplementary Fig. 6: Weight of the wireless photometry system (A), a 3-D printed transparent head protector (B), a cannula (C), and a patch cord with cannula (D) for fiber photometry System.

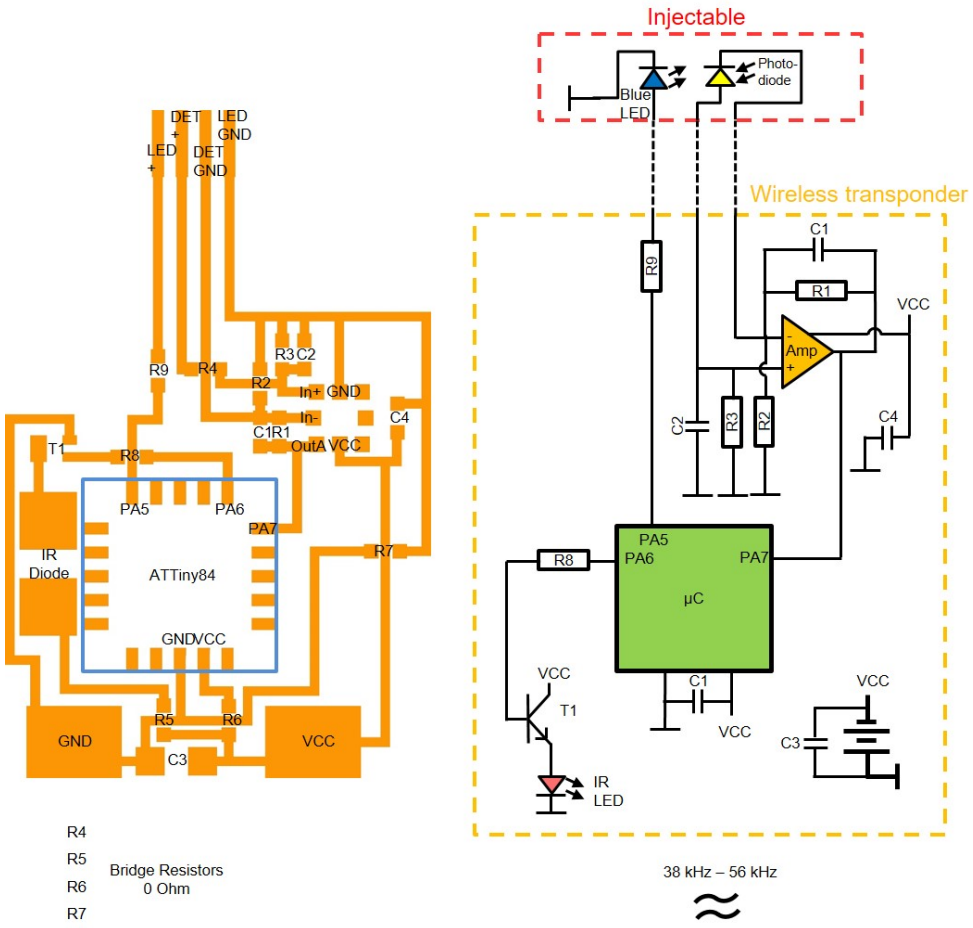

Supplementary Fig. 7: Circuit design for wireless photometry transponder and injectable.

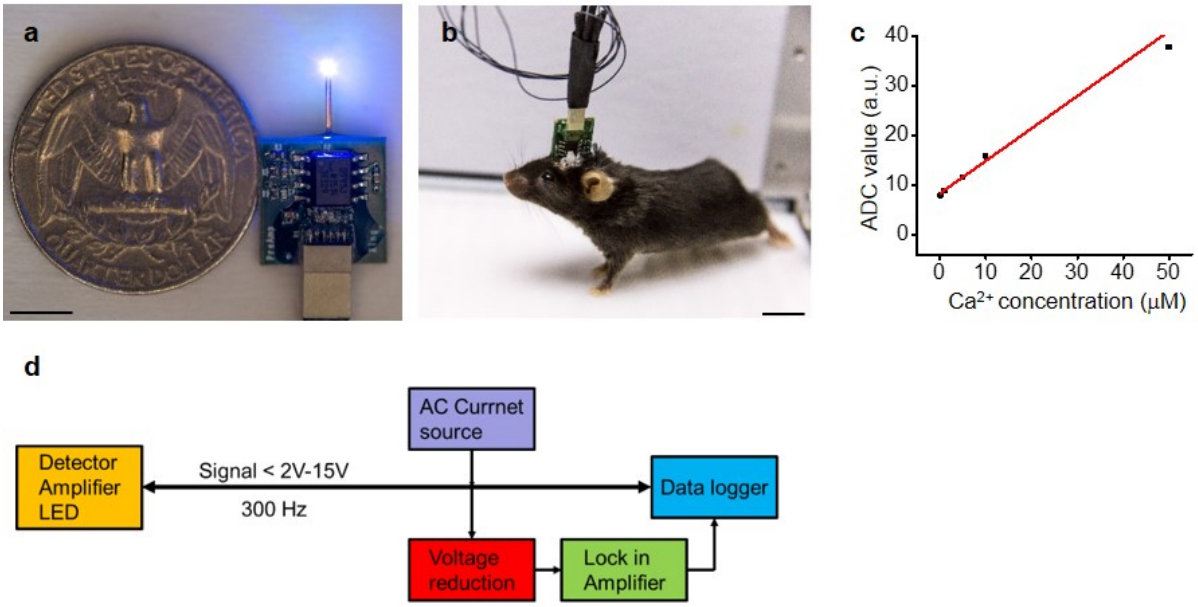

Supplementary Fig. 8: (A) Photograph of a wired photometry system next to a US quarter. Scale bar, 6 mm. (B) Photograph of a moving mouse during recording. Scale bar, 1.2 cm. (C) *In vitro* measurement of fluorescence intensity changes with different Ca^{2+} concentrations from 0.1 μM to 50 μM by the wired photometry probe. (D) Electronic working principle of the wired photometry system.

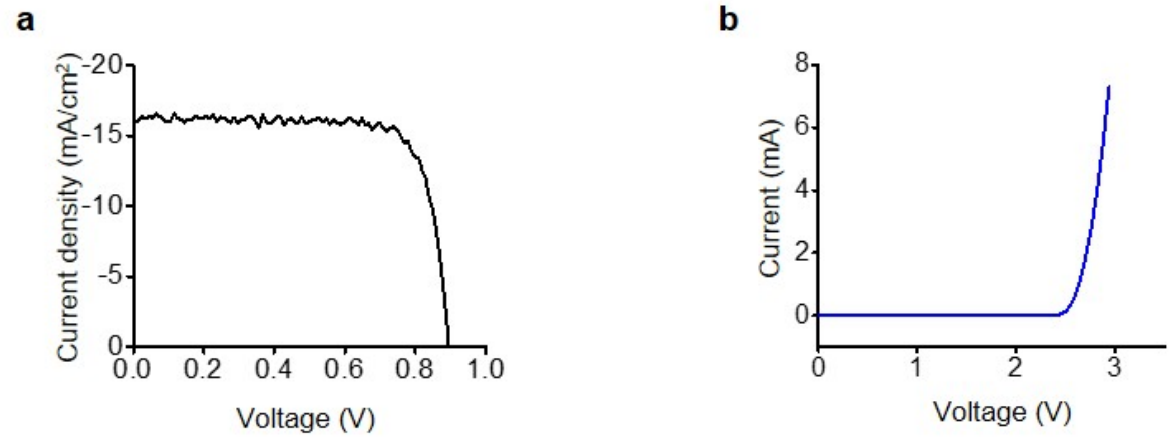

Supplementary Fig. 9: Current-voltage characterizations of μ-IPD and μ-ILED. (A) Current density versus voltage curve of a representative μ-IPD under AM 1.5 G illumination at 100 mW/cm^2. (B) Current versus voltage curve of a representative μ-ILED.

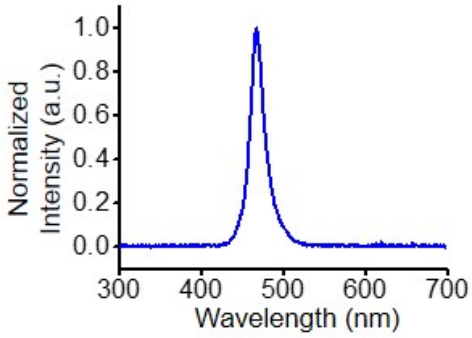

Supplementary Fig. 10: Normalized emission spectrum of an operating μ-ILED on the injectable needle.

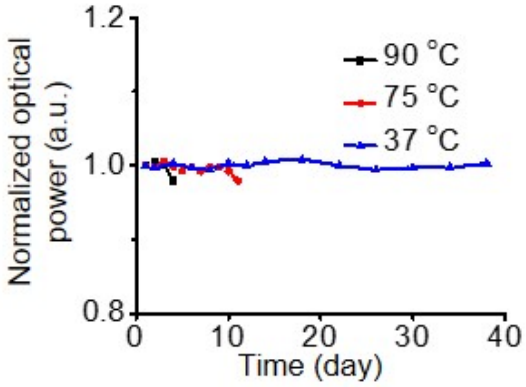

Supplementary Fig. 11: Normalized photovoltage signals from the μ-IPD at ambient condition versus function time after immersion in phosphate-buffered saline with temperatures of 90 °C, 75 °C, and 37 °C.

Supplementary Fig. 12: Image of a wireless photometry system operating after implanted in BLA region for 2 months. Scale bar, 2 mm.

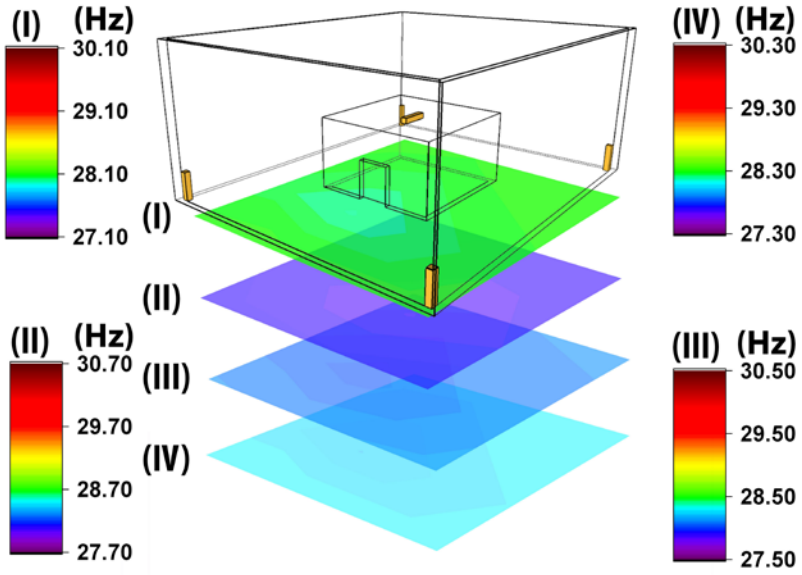

Supplementary Fig. 13: Graph displaying data rates in a 60 cm x 60 cm test cage with an opaque enclosure in the center. Receiver location is marked in orange. Data rates are recorded in Hz, counting only successful 12 bit data package transmissions, with a transponder facing in all cardinal directions. Transponder facing north (I); transponder facing east (II); transponder facing south (III); transponder facing west (IV).

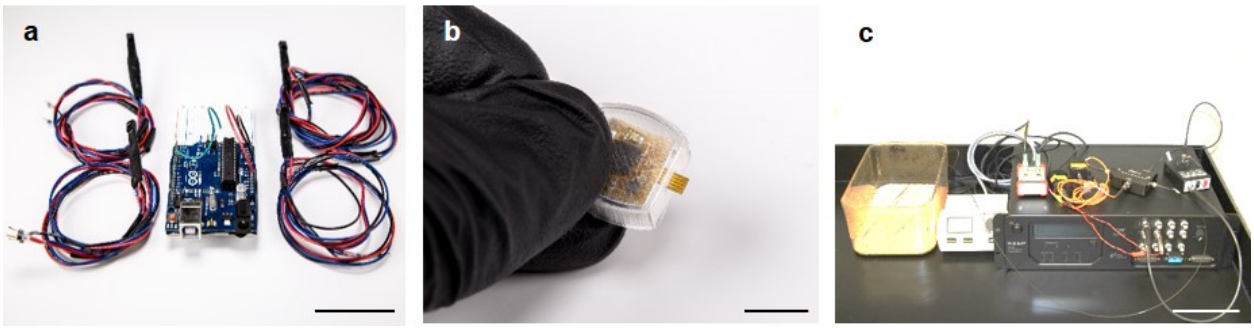

Supplementary Fig. 14: (A) Wireless receiver station with quad receiver modules. Scale bar, 5 cm. (B) Opened housing for social animal interaction recording. Scale bar, 1 cm. (C) Image of the fiber photometry system next to a home cage. Scale bar, 15 cm.

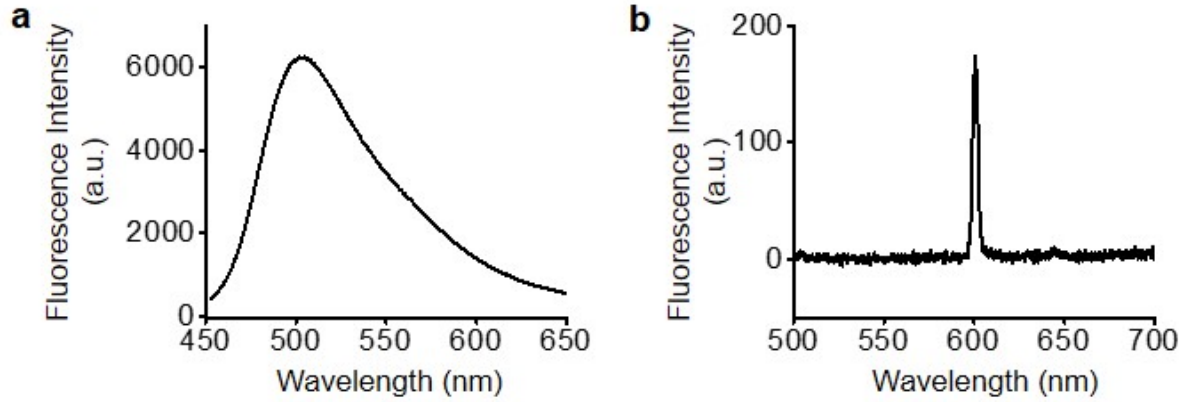

Supplementary Fig. 15: (A) Fluorescence spectrum of 0.3 μM Oregon Green® 488 BAPTA-2 calcium indicator mixed with 0.1 μM $CaCl_2$, excited at 488 nm. (B) Fluorescence spectrum of a 75 μm thick PI film excited at 488 nm.

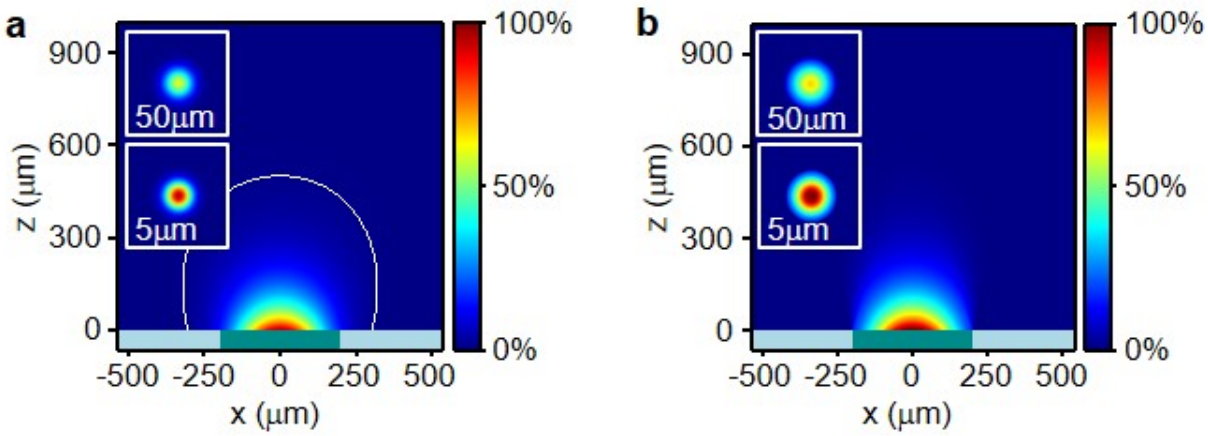

Supplementary Fig. 16: (A) Normalized emission intensity profile with 1% contour for the optical fiber as a function of depth in brain tissue. (Inset) Emission intensity at positions 5 μm and 50 μm above the optical fiber. (B) Spatial distribution of fluorescence intensity captured at the tip of the optical fiber as a function of depth in brain tissue. (Inset) Fluorescence intensity at positions 5 μm and 50 μm above the tip of the optical fiber.

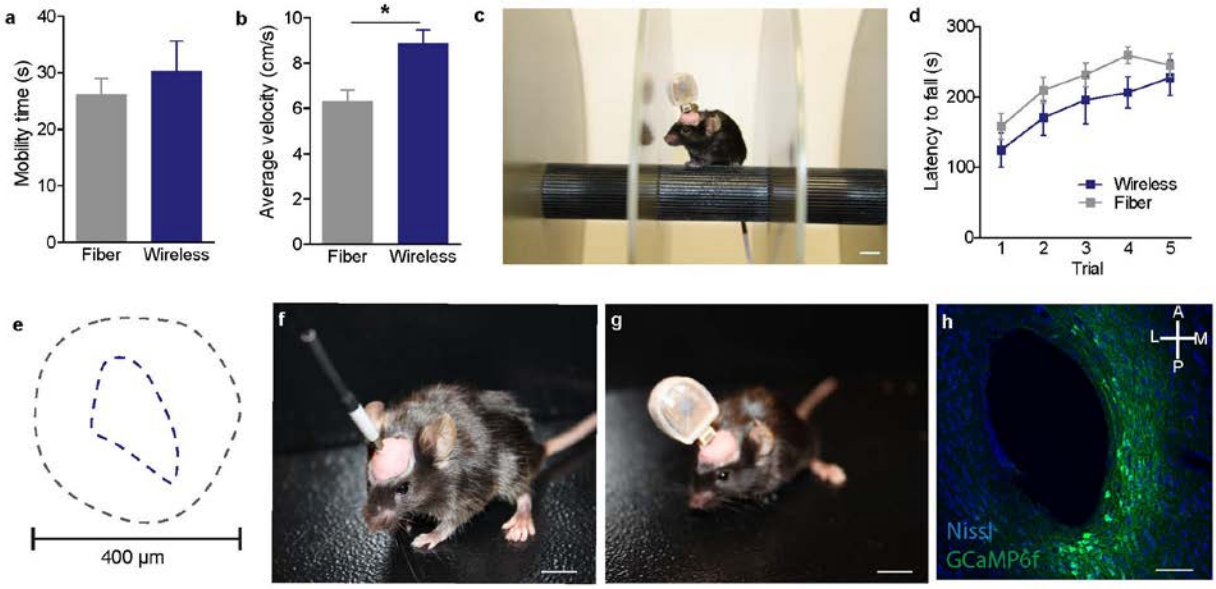

Supplementary Fig. 17: Wireless photometry systems for neural recordings in freely-behaving animals. (A) Tethered fiber-implanted and tetherless wireless-implanted mice do not differ in the amount of time immobile in the OFT. (B) Wireless-implanted mice have increased velocity during the OFT (2-tailed test, *p<0.05, n=7-9). (C) Photograph of wireless-implanted mouse performing the rotarod task. Scale bar, 1 cm. (D) Chronic implantation of the wireless devices does not alter motor coordination in a rotarod assay (n=8-10/group, 2-way ANOVA, p=.16). (E) Overlay of lesion areas resulting from chronic implantation (wireless =blue; fiber=grey). (F-G) Photograph of mouse, (F) tethered and implanted with a traditional fiber optic probe or (G) attached to the complete wireless photometry probe. Scale bars, 1 cm. (H) Confocal image of lesion at the site of recording showing expression of calcium indicator GCaMP6f around the site of the wireless photometry probe. Scale bar, 75 μm.

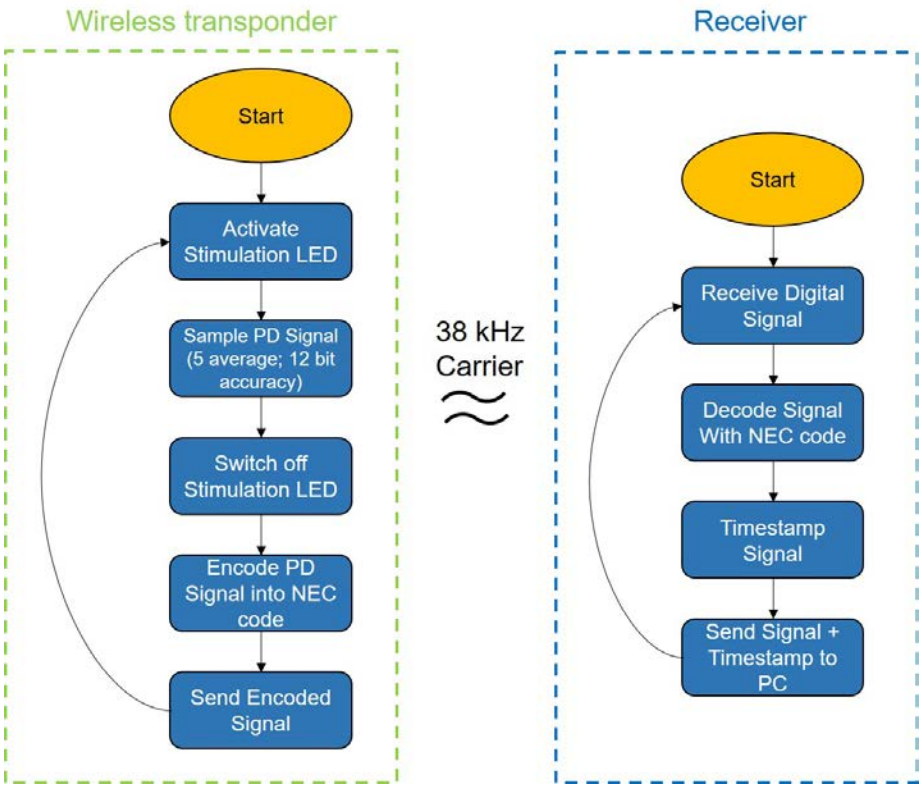

Supplementary Fig. 18: Program flow for wireless transponder and receiver.

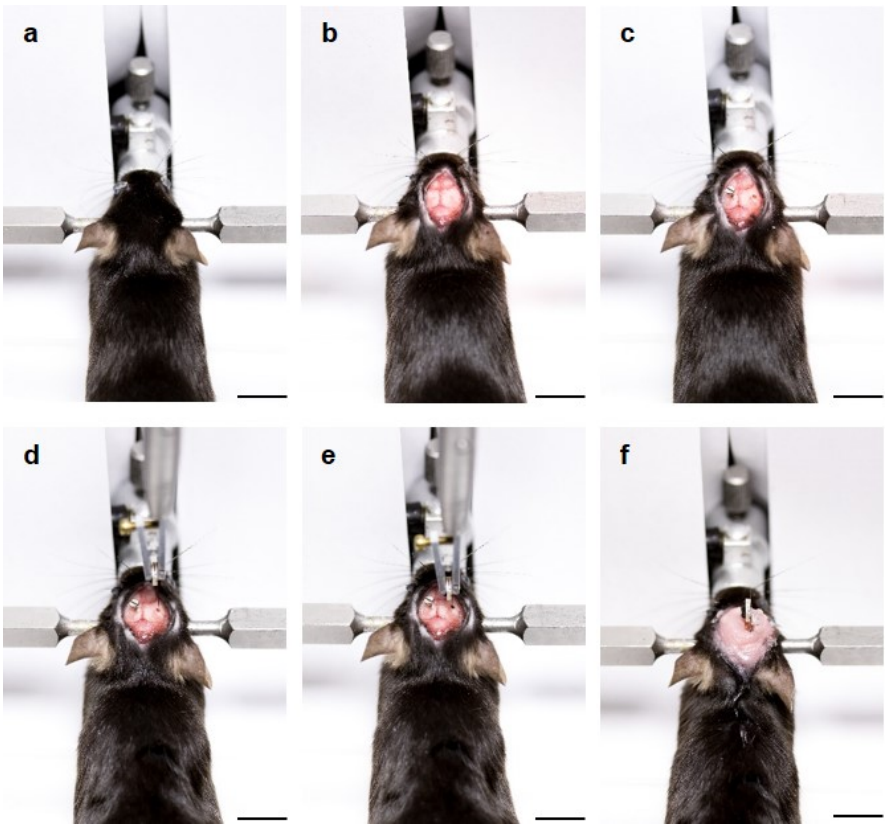

Supplementary Fig. 19: Surgery process. (A) The anesthetized mouse is head-fixed on the stereotax. (B) Fur is razed and skin is cut and opened with scalpel. (C) A hole is opened with a drill bit for probe implant, and a screw is driven into the other side of skull as support. (D) Device is delivered by a holder upon the hole. (E) Slowly low down the probe until get BLA region set by the coordinates. (F) Superglue is used to attach the device, skull and the supportive screw. Then dental cement is applied to build up a cup for further securing and protection. Scale bar, 13 mm.

	Wireless photometry device	Fiber photometry device
Probe dimension	~150 × 350 μm	400 μm diameter
Weight	29 mg for the injectable	0.43 g for the cannula
Illuminating volume	2.20×10^8 μm^3	3.77×10^8 μm^3
Maximum probing depth	360 μm	500 μm
Optical power	0-240 μW	0-21.8 mW
Noise equivalent power at 527 nm	~4.1×10^{-14} W (for the system)	~1.9×10^{-14} W (for the photoreceiver)
Numerical aperture	0.78 for illumination, and 1.35 for detection	0.48
Bending stiffness	< 1×10^{-7} $N \cdot m^2$	> 1×10^{-5} $N \cdot m^2$

Supplementary Table 1: Comparison between wireless and fiber photometry probes used.

Device	Component	Price (Dollar)
Transponder	Microcontroller	0.70
	Operational amplifier	0.50
	Passive components	0.10
	Battery	12.0
	Flex PCB	1.00
	IR LED	0.30
	3d Printed Housing	1.00
Receiver Station	Universal microcontroller board	12.0
	IR receivers (5 for extended system)	6.40
	Cables	2.00
Injectable Probe	FPC Connector	0.60
	μ-ILED	0.10
	μ-IPD	1.00
	PDMS	0.10

Supplementary Table 2: Description of cost for wireless photometry system.

Antibody	Species	Dilution	Source	Catalog No.
Anti-GFAP	Guinea Pig	1:500	Synaptic Systems	173 004
Anti-Iba1	Rabbit	1:300	Wako Chemicals	019-19741
Alexafluor 633 anti-rabbit	Goat	1:1000	Invitrogen	A21070
Alexafluor 546 anti-guinea pig	Goat	1:1000	Invitrogen	A11035
Neurotrace 435/455	N/A	1:400	Life Technologies	N21479

Supplementary Table 3: Description of antibodies used: species, dilution, and source.

Supporting Information

Lu et al. 10.1073/pnas.1718721115

Movie S1. Video of two behaving animals implanted with fiber photometry systems. These results demonstrate that fiber photometry systems introduce tethers to the animals and interfere with their interactions.

Movie S1

Movie S2. Video of two freely behaving animals implanted with wireless photometry systems. These results demonstrate that wireless photometry systems enable animals to behave in a tether-free manner.

Movie S2

Other Supporting Information Files

SI Appendix (PDF)